Lithos 352–353 (2020) 105321

Contents lists available at ScienceDirect

Lithos

journal homepage: www.elsevier.com/locate/lithos

Research article

Ages and genesis of W-Sn and Ta-Nb-Sn-W mineralization associated with the Limu granite complex, Guangxi, China

Wenting Huang [a], Jing Wu [b], Huaying Liang [a,*], Jian Zhang [a,c], Long Ren [a], Xilian Chen [a,d]

[a] Key Laboratory of Mineralogy and Metallogeny, Guangzhou Institute of Geochemistry, Chinese Academy of Sciences, 511 Kehua Street, Wushan, Guangzhou 510640, China
[b] College of Resource and Metallurgy, Guangxi University, Nanning, Guangxi 530004, China
[c] Key Laboratory of Environment Change and Resources Use in Beibu Gulf, Ministry of Education, Nanning Normal University, Nanning 530004, China
[d] State Key Laboratory of Nuclear Resources and Environment, East China University of Technology, Nanchang 330013, China

ARTICLE INFO

Article history:
Received 31 May 2019
Received in revised form 28 November 2019
Accepted 3 December 2019
Available online 10 December 2019

Keywords:
Ta-Nb-Sn-W mineralization
Evolved granite
Magmatic-hydrothermal transition
Ore-forming age
Limu

ABSTRACT

The Limu granite complex spans three granitic stages, forming the largest Indosinian Ta–Nb–Sn–W ore field in South China. There includes quartz-vein W—Sn (type-1) mineralization associated with second-stage granite, as well as Ta–Nb–Sn–W mineralization associated with third-stage granite including quartz–feldspar-vein (type-2), pegmatite dike (type-3), and disseminated (type-4) mineralization. To elucidate the magmatic evolution and genesis of these types of mineralization, we obtained muscovite $^{40}Ar/^{39}Ar$ ages, zircon LA–ICP–MS U—Pb ages, and Lu—Hf and Nd isotopic, trace-element, and geochemical compositions of the Limu granite complex. The Limu granites are peraluminous (A/CNK > 1.1) with negative εNd(t) values (−8.5 to −9.7) and T_{DM2} ages of 1780–1685 Ma, suggesting that they were derived mainly from partial melting of Paleoproterozoic basement. Remnants of Caledonian zircons (429.4 ± 5.6 Ma) indicate Caledonian granite melting in the source. Low Zr/Hf (<13) and Nb/Ta (<5) ratios and the tetrad effect in rare-earth-element patterns of the second- and third-stage granites indicate that the magmas were highly evolved and underwent late-stage exsolution of fluids. Muscovite from type-1 ore yielded an $^{40}Ar/^{39}Ar$ age of 213.7 ± 1.1 Ma. Two hydrothermal zircons and two muscovite samples from third-stage granite containing type-4 mineralization yielded similar U—Pb ages of ca. 203 Ma and $^{40}Ar/^{39}Ar$ ages of ca. 208 Ma, respectively. We conclude that type-1 mineralization was formed at ca. 214 Ma and was hydrothermal in origin, whereas Ta–Nb–Sn–W mineralization was formed at ca. 208–203 Ma and was of magmatic-hydrothermal origin. Mantle-derived heat from a long-lived magma chamber was essential for the high-temperature anatexis that formed Ta–Nb–Sn–W-rich melts, with the combined effects of crustal thickening during the Indosinian Orogeny, local delamination, asthenospheric upwelling, and deep faulting facilitating the continuous supply of heat.

1. Introduction

Ta and Nb are becoming increasingly important in modern society, and their ore forming processes are attracting greater attention (e. g., Linnen, 1998). Rocks related to Ta—Nb deposits are mainly pegmatites, granites, and carbonatite. South China is well known for large-scale granite–related rare metal mineralization (e. g., Zhang et al., 2006; Mao et al., 2011; Zhou et al., 2016; Huang et al., 2017a; Wu et al., 2018a; Xie et al., 2018). Caledonian (490–390 Ma), Indosinian (257–200 Ma), and Yanshanian (200–135 Ma) magmatism occurred in South China, with most rare-element deposits being genetically related to Yanshanian granites (Mao et al., 2007), such as in the Yichun (Wu et al., 2018a), Dajishan (Wu et al., 2017), Renli giant (Liu et al., 2018), Xiangdong, Xianghuapu, and the Xianghualing Ta—Nb deposits (Chen et al., 2008).

The Limu ore field in Guangxi Province (Fig. 1A) hosts the largest Indosinian-granite related rare-metals sources in South China, and contains three large Ta–Nb–Sn–W deposits and a series of Ta–Nb–Sn–W ore occurrences (Fig. 1B). Factors controlling the large-scale Indosinian-granite Ta–Nb–Sn–W mineralization in the Limu district are still poorly constrained. Furthermore, ores rich in W—Sn and Ta-Nb-Sn-W co-exist in the Limu ore field, unlike most other granite-related rare-metal deposits in South China, which host predominantly W but little Ta—Nb mineralization (e. g., Li et al., 2015a; Wu et al., 2017). This distinct association of W—Sn and Ta–Nb–Sn–W mineralization warrants further investigation.

Here, we describe the textures, geochemistry, and geochronology of Limu mineralized granites, including muscovite $^{40}Ar/^{39}Ar$ ages, zircon laser-ablation–inductively coupled plasma–mass spectrometry

* Corresponding author.
E-mail address: lianghy@gig.ac.cn (H. Liang).

https://doi.org/10.1016/j.lithos.2019.105321
0024-4937/

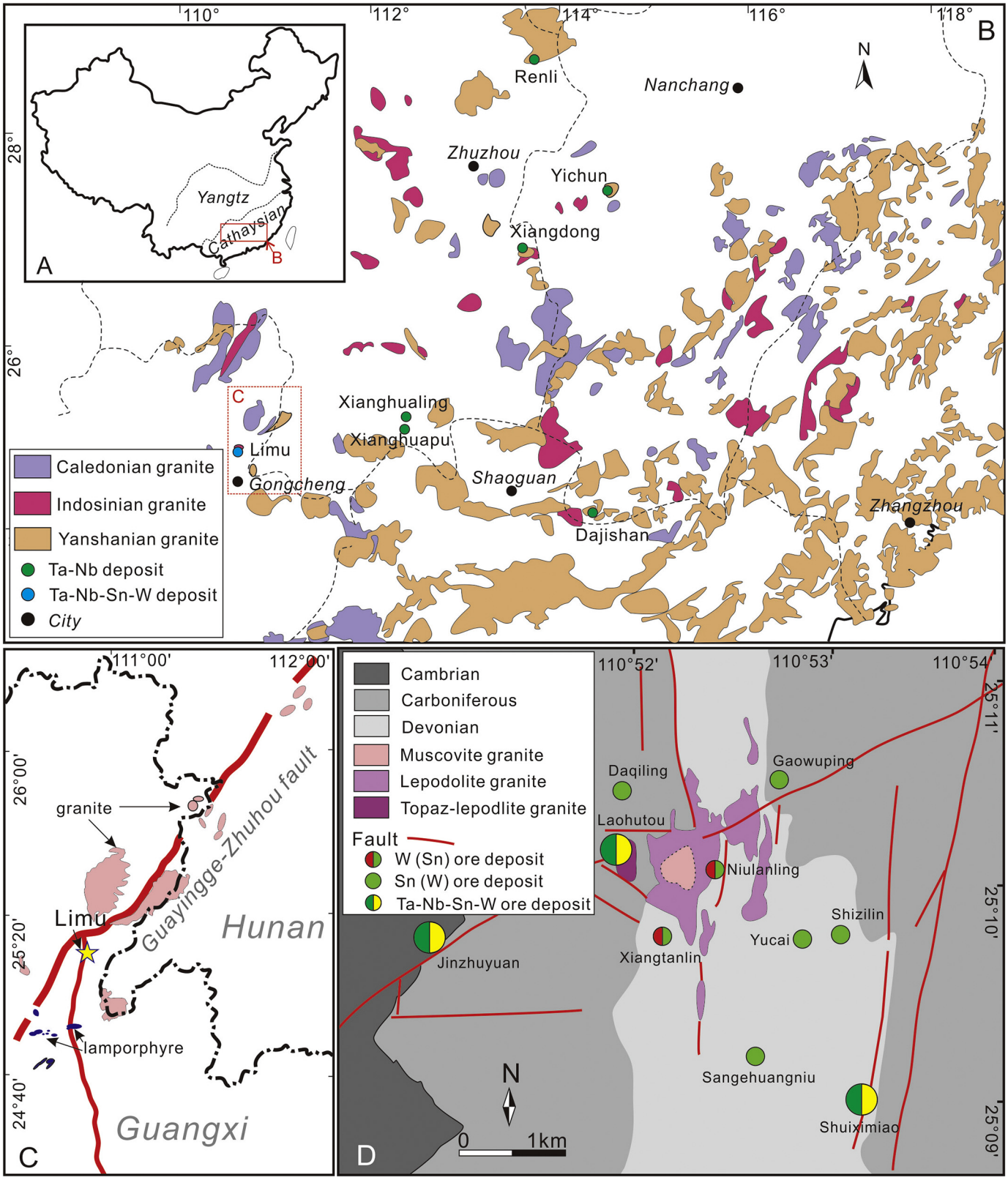

Fig. 1. (A) Sketch map showing tectonic units of South China, and location of the Nanling Range. (B) Sketch map showing granitic rocks and main Ta-Nb-Sn-W deposits in the Nanling Range (modified after Sun, 2006). (C) Sketch map showing the regional tectonic background of the Limu ore field. (D) Geological maps of the Limu ore field (modified after Dong and Ding, 2016).

(LA–ICP–MS) U—Pb ages, and Lu—Hf and Nd isotopic, trace element, and geochemical compositions of the Limu granite complex. These new data, together with results of previous studies, elucidate the relationship between magmatic evolution and the different types of mineralization, and constrain the key factors controlling formation of the abundant Ta–Nb–Sn–W deposits of the Limu ore field.

2. Geological background and ore field geology

The Limu ore field lies located at 37 km northeast of Gongcheng County, in the Guangxi Zhuangzu autonomous region of the South China Block (SCB). The SCB includes the Yangzi Block in the northwest and the Cathaysia Block (CB) in the southeast, separated by the NE-striking Jiangshan–Shaoxing Fault (Fig. 1A). The CB is composed of crystallized basement and Neoproterozoic to Mesozoic sedimentary rocks. The basement is largely Paleoproterozoic in age (2.0–1.8 Ga) and is composes greenschist- to lower-amphibolite-facies gneisses, migmatites, and plagioclase amphibolites that are un-conformably or pseudo-conformably overlain by Neoproterozoic–Mesozoic sediments. The cover sequence comprises Cambrian phyllitic mudstone and siltstone, Ordovician sandstone and siltstone, Devonian–Permian limestone and sandstone, and Triassic–Jurassic clastic rocks.

The SCB underwent three stages of magmatism: Caledonian (490–390 Ma), Indosinian (257–200 Ma), and Yanshanian (200–65 Ma) (e.g., Li et al., 2007; Li and Li, 2007; Shu et al., 2008; Wang et al., 2013a, 2013b). Yanshanian granites are more widely distributed in the CB than Caledonian or Indosinian granites, with most rare-metal deposits being genetically linked to the Yanshanian granites. The CB rare-metal deposits are distributed mainly along the E–W-trending Nanling ore belt (e. g., Guo et al., 2012; Huang et al., 2018; Li et al., 2015b; Mao et al., 2011; Mao et al., 2007).

The Limu ore field lies in the western Nanling ore belt, in the northeastern Guangxi region (Fig. 1B), which is the largest Indosinian Ta–Nb–Sn–W production area in South China. The NE-striking Guanyingge-Zhuhou fault zone, which is >550 km long and 11 km wide, traverses the ore field (Fig. 1C). A series of lamprophyres and granites occur along the Guanyingge–Zhuhou fault, indicating that it is a lithospheric fault (GXGBMR, 1985; Xu et al., 2017).

Three large-scale (Laohutou, Shuiximiao and Jingzhuyuan) and two medium-scale Ta–Nb–Sn–W deposits, as well as numerous Sn—W ore occurrences, have been found in the Limu ore field within an area of 60 km^2 (Fig. 1D). The ore field has estimated total reserves of >4300 t Ta_2O_5 with an average grade of 0.013%–0.019%, >4700 t Nb_2O_5 with a grade of 0.011%–0.014%, >50,000 t Sn with a grade of 0.21%–0.28%, and > 18,900 t WO_3 (Internal Reports of the Guangxi No. 271 geological team, 1990).

Strata in the Limu ore field contain Cambrian metamorphic sandstone, siltstone, shale, and argillaceous limestone; Devonian limestone, sandstone, and conglomerate; and Carboniferous limestone, pelite, and siliceous shale (Fig. 1D; e.g., Wang et al., 2008; Feng et al., 2013). NE–EW-trending and E–W-trending fault structures are well–developed in the Limu ore field (Fig. 1D).

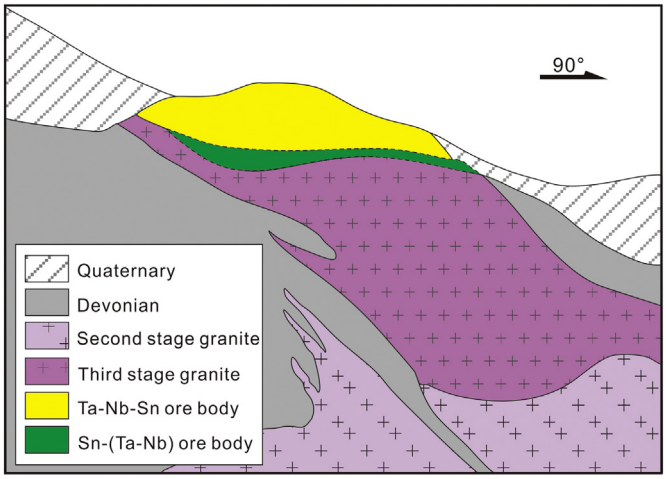

Fig. 2. Schematic vertical section of the Limu deposit (modified after Zhu et al., 2001).

The Limu granite complex occurs as stocks and dikes in the center of the ore field (e.g., Lin, 1996; Zhu et al., 2001; Fig. 2), intruding Cambrian and Devonian–Carbonaceous sediment rocks with a total surface area of ~1.5 km^2. Drill-cores indicate that these stocks and dikes are surface exposure of a concealed granite complex with an area of ~8 km^2.

The Limu granite complex spans three granitic stages (Li and Pan, 1994; Wang et al., 2008; Zhang et al., 2013; Zhu et al., 2001). The first stage crops out at Paoshuiling in the middle of the ore field with a surface area of 0.1km^2 (Fig. 1D) and comprises medium-grained porphyritic muscovite granite that has undergone strong argillaceous alteration (Fig. 3A, B). The second occurs around first-stage granite with a surface area of 1.22 km^2 (Fig. 1D, Zhang et al., 2013) and comprises medium-grained lepidolite granite and porphyritic lepidolite granite. The white lepidolite granite (Fig. 3C) has a mineral assemblage of plagioclase (andesine) (~32 vol%), perthite (~30 vol%), quartz (~31 vol%), lepidolite (~5 vol%), topaz (<1 vol%), annite (<1 vol%) (Fig. 4A). Third-stage granite occurs as a stock in the Laohutou domain with a surface area of 0.1 km^2 (Fig. 1D) and locally intrudes first-stage granite in the Paoshuiling area (Fig. 3F), with drilling having revealed two other concealed stocks in the Jinzhuyuan and Shuiximiao areas (west and southeast of Laohutou, respectively) (Fig. 1D, Zhang et al., 2013). It has a fine–medium-grained texture (Fig. 3E), with fine-grained euhedral albite crystals being locally hosted (entrapped) by large-grained xenomorphic quartz crystals (Fig. 4C), suggesting that the albite crystallized under sub-solidus quartz conditions. Third-stage granite comprise plagioclase (albite–oligoclase; 38–48 vol%), K-feldspar (20–28 vol%), quartz (22–34 vol%), lepidolite (3–5 vol%) and topaz (<3 vol%) (Fig. 4B-F), and can be classified as topaz-bearing lepidolite granite ("topaz-lepidolite granite").

Mineralization in the Limu ore field can be divided into four types: (1) W—Sn quartz-vein mineralization; and (2) quartz–feldspar vein, (3) granite–pegmatite dike, and (4) disseminated Ta–Nb–Sn–W mineralization (e.g., Li and Pan, 1994; Liang et al., 2017; Lin, 1996).

The quartz–vein W—Sn mineralization (type-1) occurs in second–stage granite and in the contact zone around it. Sixty W—Sn quartz veins have been found in the Niulanping, Xiantanling, and Sangehuangniu domains of the Limu ore field, with lengths of 60–80 m and thicknesses of 0.3–1 m. They have proven total reserves of 11,041 t WO_3 and 7895 t Sn, with a WO_3/Sn ratio of 1.40.

The other three types of mineralization are closely associated with third-stage topaz-lepidolite granite.

The quartz–feldspar vein mineralization (type-2) occurs in the Shuiximiao and Sangehuangniu areas, mainly in fractures in Devonian limestone and marble covering the upper third-stage granite. Alteration includes carbonate re-crystallization, fluoritization, and lepidolitization.

The granite–pegmatite dike mineralization (type-3) occurs in the Shuiximaio area, in fractures in Devonian limestone or marble around third-stage topaz-lepidolite granite.

The disseminated Ta–Nb–Sn–W mineralization (type-4) occurs mainly in the Laohutou, Shuiximaio, Jingzhuyuan, and Shiziling areas (Fig. 1D) where orebodies occur on top of third-stage granite, with an area of 750 m × (330–480) m and thickness of 2–80 m (Zhu et al., 2001). Type-4 can be divided into Ta–Nb–rich and Ta–Nb–poor domains on the basis of Ta—Nb and Sn—W contents, with the former usually occurring in the middle of orebodies and the latter on the margins, and with the former having lower Sn contents compared with the latter (Table 1). Columbite–tantalite crystals occur with K-feldspar and albite, or are semi-enclosed by quartz (Fig. 4C). No alteration or reaction rims have been found among columbite–tantalite, albite, or quartz.

Ore grade and reserves of the different mineralization types are given in Table 1. The main ore minerals include cassiterite, tantalum niobite, niobite, tantalum, rutile, wolframite, huebnerite, scheelite, and associated arsenopyrite, pyrrhotite, magnetite, chalcopyrite, pyrite, bismuthinite, and molybdenite. Gangue minerals include feldspar, quartz, muscovite, fluorite, and topaz. Some Ta and Nb minerals are hosted as inclusions in cassiterite.

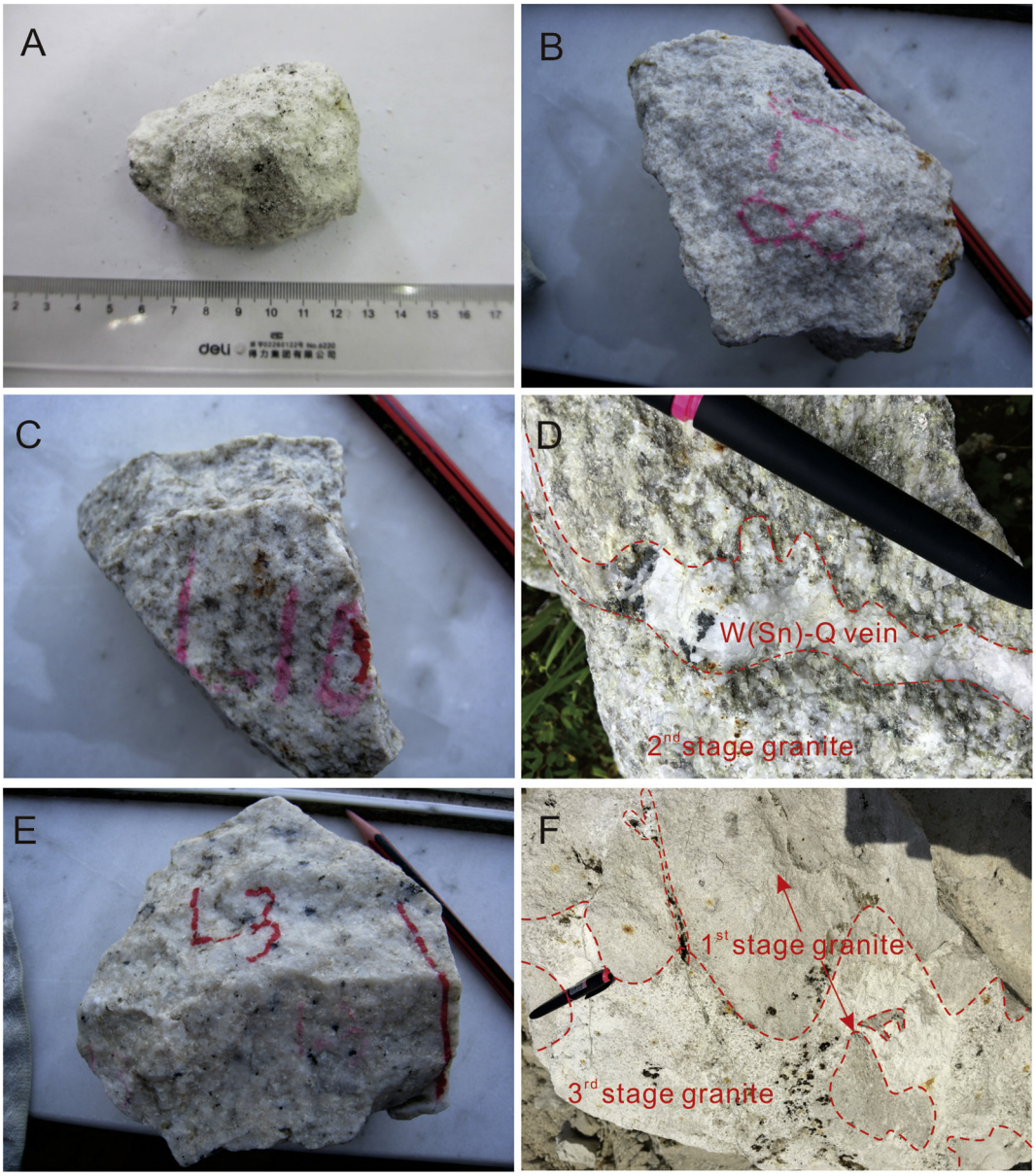

Fig. 3. Representative photographs of (A) rock with strong kaolinization alteration; (B) muscovite granite; (C) lepidolite granite; (D) quartz-vein W—Sn ores hosting in the lepidolite granite; (E) topaz-lepidolite granite; (F) the contact relationship between third-stage topaz-lepidolite granite and the first-stage muscovite.

3. Samples and analytical methods

3.1. Zircon U—Pb dating and trace-element compositions

One sample of first-stage muscovite granite from the Paoshuiling area (sample L-7), and two of third-stage topaz-lepidolite granite from the Shuiximiao (sample LM-2) and Laohutou (sample LM-3) areas were collected for U—Pb dating and trace-element analysis. Zircons from a first-stage granite sample with strong kaolinization (sample LM-1, Fig. 3A) were also selected for U—Pb dating.

Zircons were separated from ~2 kg of crushed and sieved samples using conventional heavy-liquid and magnetic separation techniques. Euhedral, clear zircon grains were hand-picked under a binocular microscope, and >100 grains were mounted in epoxy resin and polished. Zircon internal structures were imaged by cathodoluminescence (CL) before isotopic analysis.

Single zircon grains were analyzed by LA-ICP-MS at the State Key Laboratory of Isotope Geochemistry, Guangzhou Institute of Geochemistry, Chinese Academy of Sciences (GIG–CAS), Guangzhou, China, using procedures described by Tu et al. (2011) with 31 μm spots, a repetition rate of 8 Hz, and a beam flux of 8 Jcm^{-2}. US National Institute of Standards and Technology (NIST) standard reference material (SRM) 610 (Jochum et al., 2011; Pearce et al., 1997) and Temora zircon (Black et al., 2003) were used as external standards.

Off-line inspection and integration of background and analytical signals and quantitative calibrations for trace-element analyses and U—Pb dating, were performed using ICPMSDataCal software (Liu et al., 2010). Concordia diagrams were plotted and associated weighted-means ages calculated using Isoplot/Ex_ver3 (Ludwig, 2003). Data with >10% discordance in $^{206}Pb/^{238}U$ versus either $^{207}Pb/^{235}U$ or $^{208}Pb/^{232}Th$ plots were excluded from age calculations (Liang et al., 2006). Cumulative probability plots were used to identify Pb inheritance and loss (Zou et al., 2017). Zircons mostly exhibited a linear distribution with a positive slope in cumulative probability plots, with outliers above and below the line representing inherited cores and Pb loss, respectively.

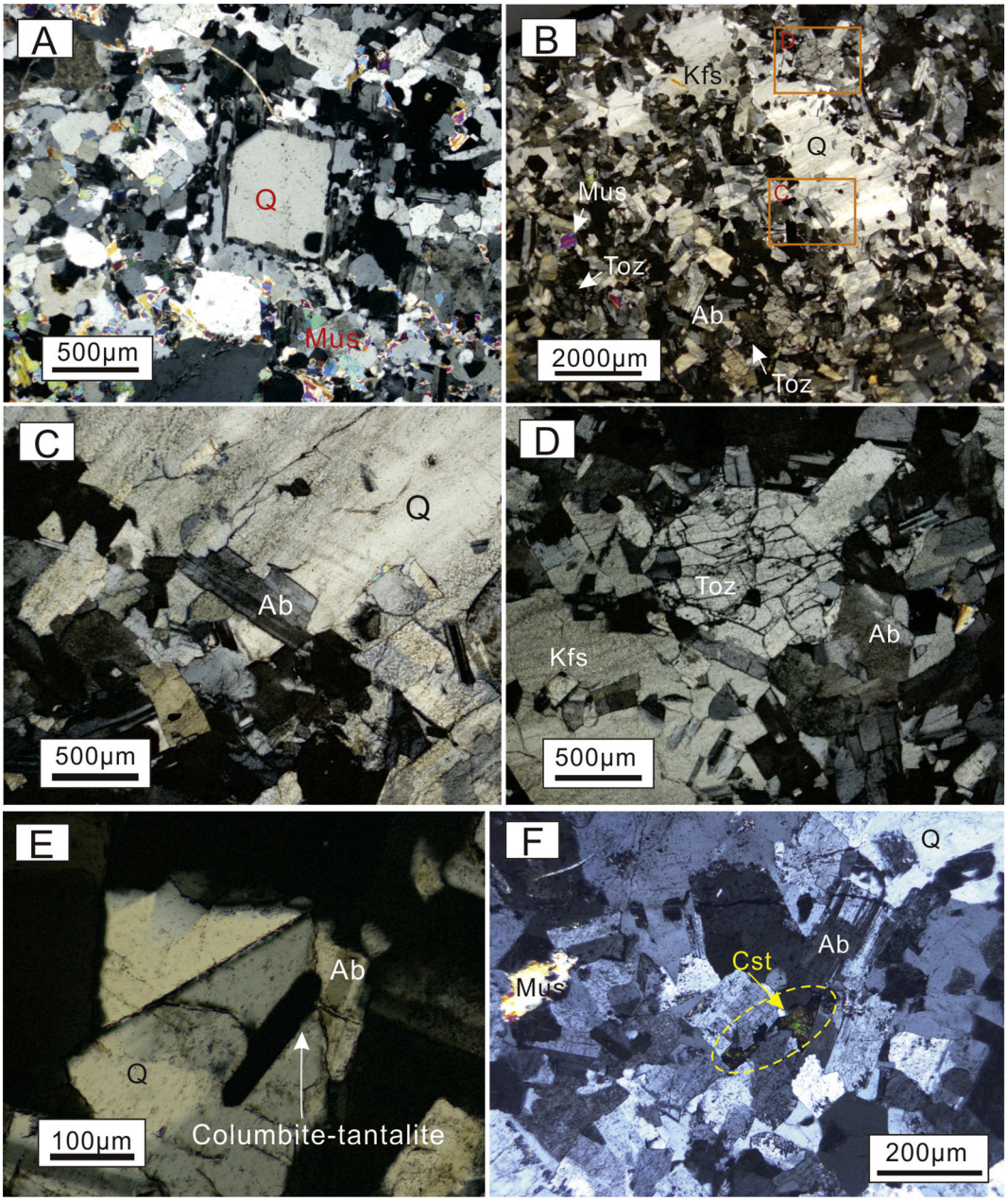

Fig. 4. Representative transmitted-light photomicrographs of (A) quartz-K feldspar-plagioclase-lepidolite assemblage of second-stage lepidolite-granite; (B) quartz-albite-K feldspar-lepidolite-topaz assemblage of third-stage topaz-lepidolite granite; (C) close up view of albite entrapped in a large grained xenomorphic quartz crystal; (D) close up view of topaz in topaz-lepidolite granite; (E) columbite-tantalite crystal semi-enclosed by quartz; (F) cassiterite crystal in the K-feldspar and albite. Abbreviations: Ab = albite, Cst = cassiterite, Kfs = K-feldspar, Mus = muscovite, Q = quartz, Toz = topaz.

Such outliers were excluded from U—Pb age and mean–square–weighted–deviation (MSWD) calculations.

3.2. Muscovite $^{40}Ar/^{39}Ar$ dating

One muscovite sample from type-1 ore (sample LM-20) and two from third-stage topaz-lepidolite granite (samples L-6 and L-11) were selected for $^{40}Ar/^{39}Ar$ dating, with muscovite being hand-picked from crushed samples. Muscovite (~50 mg) samples were irradiated for 24 h in channel B4 of the Beijing 49–2 reactor at the Chinese Academy of Nuclear-Energy Sciences, Beijing, China. Muscovite standard ZBH-25 (132.7 Ma; Sang et al., 2006) was used to monitor neutron flux.

Total-fusion analyses were performed by MS (Isoprobe VG 5400, Isotopx, United Kingdom) at GIG–CAS. Detailed analytical methods and data correction procedures were as described by Qiu and Wijbrans (2006). Data processing was performed using ArArCALC 2.4 software (Koppers, 2002), and $^{40}Ar/^{36}Ar$–$^{39}Ar/^{36}Ar$ isochron diagrams were plotted using Isoplot 4.0 (Ludwig, 2003).

3.3. Major- and trace-element analyses

Two samples of first-stage muscovite granite (samples L-7 and L-8), four of second-stage lepidolite granite (samples L-10 to L-13), and five of third stage topaz-lepidolite granite (samples L-1 to L-4, L-6, L3–2, and L4–2) were selected for analysis. After removal of weathering rinds, 100 g of each sample was crushed to 200 mesh in a jade mill. Major- and trace-element analyses were conducted at GIG-CAS.

For major-element analyses, samples were fluxed with $Li_2B_4O_7$ (1:8) to make homogeneous glass disks at a temperature of ~1200 °C. The

Table 1
Main characteristic of the three stages granites and associated mineralization in Limu ore field.

Rock type	Mineral assemblage	Age (Ma)	Associated Ore type	Estimated reserves	Domains		Grade				Ta_2O_5/Nb_2O_5	WO_3/Sn
							Ta_2O_5	Nb_2O_5	Sn	WO_3		
First stage porphyritic muscovite granite	Plagioclase, quartz, K-feldspar, muscovite	ca. 230	–		Paoshuiling		–	–	–	–	–	–
Second stage lepidolite granite	Andesine, perthite, quartz, lepidolite, and minor topaz (< 1vol %)	ca. 225 to ca. 214	Quartz vein type W-Sn	7895 t Sn, 11,041 t WO_3	Niulanping, Xiantanling, and Sangehuangniu							1.40
Third stage topaz-bearing lepidolite granite	Albite-oligoclase, K-feldspar, Quartz, lepidolite, and topaz (<3 vol%).	ca. 210 to ca. 203	Pegmatite or Keldspar-quartz vien type Ta-Nb-Sn-W	Ta_2O_5 > 4300 t, Nb_2O_5 > 4700 t, Sn > 42,186 t, WO_3 > 3300 t	Shuiximiao		0.0188%	0.0138%	0.135%	0.011%	1.36	0.08
			Ganite disseminated type Ta-Nb-Sn-W		Laohutou		0.0126%	0.0103%	0.205%	0.025%	1.12	0.12
					Shuiximiao	Ta-Nb rich	0.0104%	0.0114%	0.113%	0.013%	0.91	0.12
						Ta-Nb poor	0.0079%	0.0087%	0.260%	0.023%	0.91	0.09
					Jinzhuyiang	Ta-Nb rich	0.0145%	0.0117%	0.054%	0.007%	1.24	0.13
						Ta-Nb poor	0.0072%	0.0081%	0.280%	0.011%	0. 89	<0.01

Data of ore grade (%) or total reserves (t) are from Li and Pan (1994), Wang et al., (2008) and the internal reports of the Guangxi No. 271 geological team.
Age data are from Feng et al. (2013), Feng et al. (2019), Ma et al. (2013), Yang et al. (2009), Zhang et al. (2013), and Zhang et al. (2014).

dikes were analyzed by wavelength-dispersive X-ray fluorescence (Rigaku ZSX 100e) with relative standard derivations of <5%.

For trace-element analyses, the powered samples were digested in HF + HNO_3 in Teflon bombs at 100 °C for 7 d (Liu et al., 1996). Trace-elements compositions were determined by ICP–MS (Perkin-Elmer Sciex ELAN 6000). Standards GSR-1, BHVO-2, and OU-6 were used as reference materials, and pure Rh standard solutions for internal calibration. Analytical precision was better than 3%.

3.4. Bulk–rock Nd isotopic compositions

Nd isotopic compositions of samples from the first (samples L-7 and L-8) and second (samples L-10, L-12, and L-13) stages of Limu granites were determined. Powdered samples were dissolved HF + HNO_3 in Teflon bombs. Rare-earth-elements (REEs) were separated by cation-exchange chromatography using procedures of Wei et al. (2002). Nd isotopic ratios were determined by multicollextor (MC) –ICP–MS (VG-354) at GIG-CAS using procedures described by Liang et al. (2003). The mass-fractionation correction was based on $^{156}Nd/^{144}Nd$ = 0.7219 Shin Etsu JNdi-1 was used as a standard with $^{143}Nd/^{144}Nd$ = 0.512090 ± 0.000003 (2σ; n = 3).

3.5. Zircon Lu—Hf isotopic compositions

Zircon Lu—Hf isotopic compositions of first-stage granite (sample L-7) were determined by MC–ICP–MS (Thermo Fisher, Finnigan Neptune) with a RESOlution M50 laser-ablation system at GIG-CAS, with 40 μm ablation pits, 30 s ablation time, 8 Hz repetition rate, and beam flux of 4 J cm^{-2}. Procedures were as described by Wu et al., 2006 and (Zhang et al., 2015). Penglai zircons were used as the standards. The measured $^{176}Hf/^{177}Hf$ ratios of 0.282918 ± 0.000035 (2σ; n = 25) is consistent with the certified ratio of 0.282906 ± 0.000010 (2σ) (Li et al., 2010).

4. Results

4.1. Zircon morphology, trace-element compositions, and U—Pb ages

Representative zircon images are shown in Fig. 5. Their trace-element compositions are given in Appendix 1, and U—Pb dating results in Appendix 2. Analyses of zircons from samples LM-1, −2, −3, and −7 are described separately here.

Zircons from sample LM-1, with strong kaolinization are euhedral and display clear oscillatory zoning in CL images (Fig. 5A), consistent with a magmatic origin (Hoskin, 2005). These zircons have Hf, total REE (∑REE), and Y contents of 7848–11,176 ppm of 919–3595 ppm, and 1115–4240 ppm, respectively, with mean Nb and Ta contents of 7.59 ppm and 4.69 ppm, respectively. Twenty-one of these zircons were selected for U—Pb dating. Fourteen zircons with concordance of >90% have U contents of 1069–6066 ppm with Th/U ratios of 0.02–0.72. Anomalous ages of two zircons (77.3 ± 0.8 Ma and 1677.3 ± 12.6 Ma) were attributed to Pb loss and an inherited zircon, respectively. The remaining 12 zircons yielded a U—Pb age range of 411.9 ± 3.3 to 457.7 ± 6.9 Ma with a weighted-mean age of 430.7 ± 7.7 Ma (MSWD = 12.40; Fig. 6A; Appendix 2). The high MSWD value implies that analysis spots may encompass different age groups. In a cumulative probability plot (Fig. 6A), the four points at the extremes of the range indicated possible Pb loss or inheritance and, with exclusion of these points, the remaining eight zircons yielded a weighted-mean age of 429.4 ± 5.6 Ma (MSWD = 6.20).

Most zircons from the first-stage muscovite granite (sample L-7) are euhedral and characterized by dark rim overgrowth of bright cores or overall darkness in CL images (Fig. 5B). These zircons have mean Hf, Nb, Ta, and Ca contents of 47,862 ppm, 69.9 ppm, 131 ppm, 501 ppm, repectively, higher than those of the Caledonian zircons of sample LM-1. Their mean Th and U contents (269 and 1383 ppm) are also higher, but their mean ∑REE and Y contents (1840 and 2379 ppm) are lower. Twenty-five LA–ICP–MS U—Pb analyses were performed on these zircons. Four zircons with concordance <90% were excluded from calculations, with the remaining 21 zircons yielding Th/U ratios of 0.01–0.78. One zircon yields an age of 564.5 ± 20.0 and is clearly an inherited zircon. The remaining 20 zircons yielded U—Pb ages of 206.0 ± 4.6 to 249.1 ± 4.6 Ma (Appendix 2) with a weighted-mean age of 227.6 ± 5.4 Ma (MSWD = 6.5). A cumulative probability plot (Fig. 6B) indicates four extreme spots with Pb loss or inheritance and, with the exclusion of these points, the remaining 16 zircons constrain the U—Pb age of muscovite granite to 227.7 ± 4.5 Ma (MSWD = 3.27).

Zircons from the third-stage topaz-lepidolite granites (samples LM-2 from Shuiximiao and LM-3 from Laohutou) appear fairly opaque and re-brown in transmitted light, with no oscillatory growth zonation

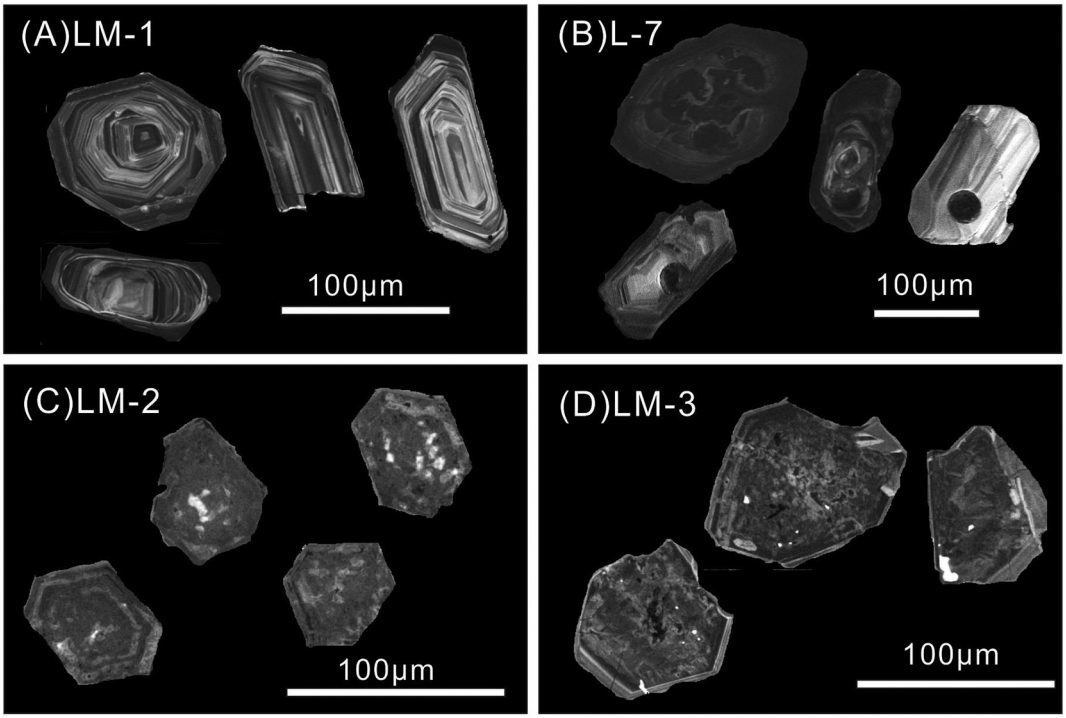

Fig. 5. CL images of representative zircons (A) from rock with strong kaolinization alteration; (B) from the muscovite granite, and (C, D) from the topaz-lepidolite granite. Sample number are shown at the top left of each panel.

visible in CL images (Fig. 5C, D). They have mean Hf, Nb, Ta, and Ca contents of 64,994 ppm, 228 ppm, 588 ppm, and Ca 3493 ppm, respectively, higher than those of zircons from first-stage muscovite granite. Their ∑REE and Y contents are very low, averaging 14.8 ppm and 11.3 ppm, respectively.

LM-2 zircons have U contents of 774–16,467 ppm with Th/U ratios of 0.02–0.20 (Appendix 2). Of the 25 analysis spots, 12 have concordances of >90%, with U—Pb ages of 161.8 ± 1.8 to 211.7 ± 2.5 Ma, of which 4 Pb-loss cases are identified in a cumulative probability plot (Fig. 6C). The remaining eight zircons yielded ages of 196.2 ± 1.9 to 211.7 ± 2.5 Ma with a weighted -mean age of 202.9 ± 3.8 Ma (MSWD = 4.94).

LM-3 zircon compositions are similar to those of LM-2 zircons, with U contents of >3150 ppm and Th/U ratios of 0.02–1.45 (Appendix 2). Fourteen of the 25 analyzed spots have concordances of >90% with U—Pb ages of 184.8 ± 10.1 to 218.1 ± 2.2 Ma, including one case each of Pb loss and inheritance indicated in a cumulative probability plot (Fig. 6D). The remaining 12 analyses yielded ages of 195.5 ± 2.3 to 212.4 ± 2.0 Ma with a weighted-mean age of 203.1 ± 3.0 Ma (MSWD = 5.65).

4.2. Muscovite $^{40}Ar/^{39}Ar$ ages

Results of $^{40}Ar/^{39}Ar$ analyses of muscovite grains from the type-1 ore (sample LM-20) and topaz-lepidolite granites (samples L-6 and L-11) are presented in Appendix 3 and illustrated in Fig. 7.

Stepwise heating of muscovite sample LM-20 produced a flat age spectrum with a main plateau comprising 11 successive steps with 98.62% of ^{39}Ar released, yielding an $^{40}Ar/^{39}Ar$ plateau age of 214.08 ± 1.05 Ma (MSWD = 1.44; Appendix 3; Fig. 7A) consistent with the corresponding isochron age of 213.66 ± 1.10 Ma (MSWD = 1.11; Fig. 7B). The initial $^{40}Ar/^{36}Ar$ ratio of 348.2 ± 46.6 (Fig. 7B) is higher than the atmospheric Ar ratio of 295.5 (Renne et al., 2009), indicating that the muscovite includes some inherited or excess ^{40}Ar, with the plateau age thus representing the oldest possible muscovite crystallization age.

Sample L-6 yielded an $^{40}Ar/^{39}Ar$ plateau age of 208.82 ± 1.02 Ma (MSWD = 0.39) with 91.52% of ^{39}Ar released over 11 steps age heating steps (Fig. 7C), identical within error to the corresponding isochron age of 208.37 ± 1.23 Ma (MSWD = 0.28; Fig. 7D). The initial $^{40}Ar/^{36}Ar$ ratio of 322.8 ± 41.4 is within error of the atmospheric Ar ratio, suggesting that the muscovite age may be considered as being 208.82 ± 1.02 Ma.

Sample L-11 yielded an $^{40}Ar/^{39}Ar$ plateau age of 208.16 ± 1.01 Ma (MSWD = 0.25) with 96.91% of ^{39}Ar released over 12 heating steps (Fig. 7E), consistent with the isochron age of 208.01 ± 1.04 Ma (Fig. 7F). The initial $^{40}Ar/^{36}Ar$ ratio of 307.5 ± 28.26 (Fig. 7F) is similar to the atmospheric Ar ratio, indicating that the muscovite did not include substantial inherited or excess ^{40}Ar and that, the plateau age of 208.16 ± 1.01 Ma is a reliable crystallization age for the muscovite.

4.3. Major- and trace-elements compositions

Major- and trace-element compositions of muscovite granite, lepidolite granite, and topaz-lepidolite granite are listed in Table 2 and shown in Figs. 8 and 9. The trace element compositions of reference materials and replicate samples are listed in Appendix 4.

All of the samples have high SiO_2 and Al_2O_3 contents with variable but low MnO and TiO_2 contents (Table 2, Fig. 8), indicating that their magmas were highly evolved.

The two analyzed first-stage muscovite granite samples (L-7 and L-8) have loss-on-ignition ratios of 2.38 and 3.27 wt% (Table 2), indicating late-stage alteration. Their highly variable SiO_2, K_2O, and N_2O contents (Fig. 8D) therefore cannot be considered as representing the original magma. Therefore, only immobile and insoluble elements, such as REEs are considered here for the first-stage granites. Their chondrite-normalized REE patterns are shown in Fig. 9A with $(La/Yb)_N$ ratios of 7.59 and 9.92 and Eu_N/Eu^* ratios of 0.27 and 0.5.

The four analyzed second-stage lepidolite granite samples have similar SiO_2, CaO, Fe_2O_3, Al_2O_3, Na_2O, and K_2O contents (Table 2, Fig. 8), with A/CNK ratios of >1.57 indicating peraluminous affinity (Fig. 8D). Their mean Nb and Ta contents are 32.01 ppm and 15.62 ppm, respectively, with Nb/Ta ratios of 1.25–3.42, whereas Zr/Hf ratios are

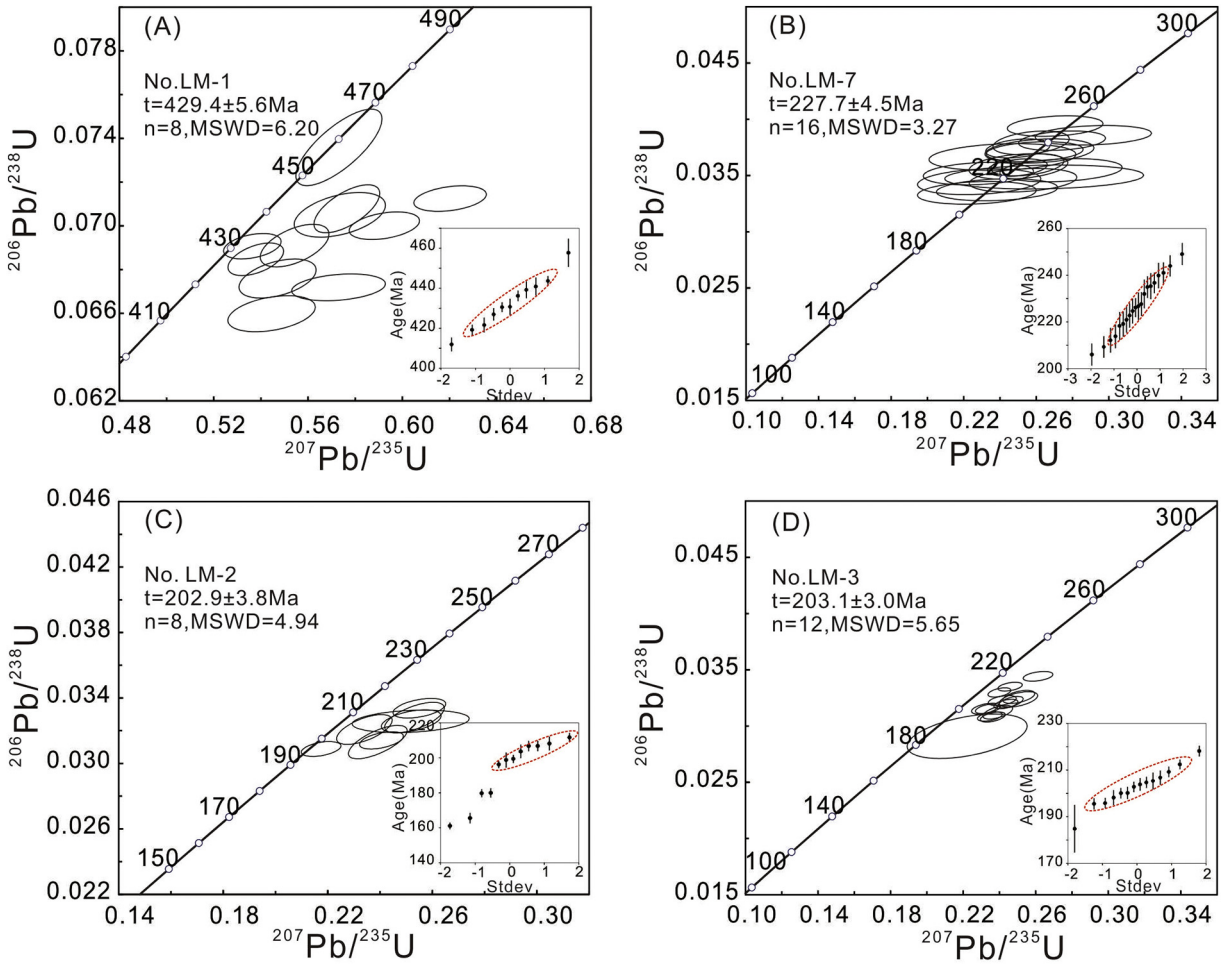

Fig. 6. U—Pb concordia diagrams of the zircons from (A) Rock with strong kaolinization alteration. (B) Lepidolite granite. (C) Lepidolite granite and (D) topaz-lepidolite granite.

10.6–13.0 (Table 2). They have ∑REE contents and $(La/Yb)_N$ ratios that are substantially lower than those of first-stage granite (Table 2), show pronounced negative Eu anomalies, and display the tetrad effect in their chondrite-normalized REE patterns (Fig. 9C).

The five analyzed third-stage topaz-lepidolite granite samples have similar SiO_2 content to that of second-stage granite, with higher Na_2O and Al_2O_3 contents and lower CaO and Fe_2O_3 contents (Table 2, Fig. 8). Their A/CNK ratios of 1.47–1.62 indicate a peraluminous affinity (Fig. 8D). They have higher Nb and Ta contents (Fig. 8F) and lower Nb/Ta ratios than those of first- and second-stage granites (Table 2, Fig. 8G, H), with Nb—Ta mineralization occurring in third-stage granite (Fig. 4E). Their Zr/Hf ratios are lower than those of second-stage granite (Fig. 8G), and their REE contents are so low that in most samples they were below detection limits (Table 2). Only one sample yielded a reliable ∑REE content of 3.26 ppm, with $(La/Yb)_N$ and Eu_N/Eu^* ratios of 1.26 and 0.04, respectively, and a strong tetrad effect (Fig. 9E).

4.4. Bulk-rock Nd isotopic compositions

Bulk-rock Nd isotopic compositions of the Limu granites are listed in Table 3 and plotted in Fig. 10A.

4.5. Zircon Lu—Hf isotopic compositions

First-stage muscovite granite zircon Hf isotopic data are listed in Appendix 5 and plotted in Fig. 10B.

5. Discussion

5.1. Sources and evolution of Limu granite complex

5.1.1. Sources

The three stages of granites in the Limu district have a close temporospatial relationship and similar bulk-rock Nd isotopic compositions, with εNd(t) values of first-stage granites being virtually identical to those of the second stage granite (−8.5 to −9.7 and −9.0 to −9.1, respectively). This suggests that granites in the Limu district were derived from a common source. The calculated T_{2DM} ages for the Limu granites have a narrow range (1780–1685 Ma; Table 3), indicating that the magmas were sourced from Paleoproterozoic crust, as supported by the zircon Hf isotopic compositions of first-stage granite, which yielded a T_{2DM} age of 2171–1618 Ma (Appendix 5).

The age of Caledonian magmatic zircons (429.4 ± 5.6 Ma; Fig. 6A) in a strongly kaolinized sample (LM-1) of first-stage muscovite granite is similar to that of Caledonian granites cropping out widely in the Nanling region (Chen et al., 2018; Li et al., 2015b; Wu et al., 2012), indicating that Caledonian granitic magmatism was also present at depth in the Limu area. The Caledonian zircons may have been captured by Indosinian magmas ascending through enclaves of the Caledonian granites, or may have been derived from partially melted Caledonian granite being involved in the formation of the Indosinian magmas. The former seems unlikely because there are no Caledonian granite outcrops out in the Limu district, and Caledonian zircons have only rarely been reported from the Limu granites. The latter suggestion seems more likely, with the zircons being relicts of Caledonian granites that were

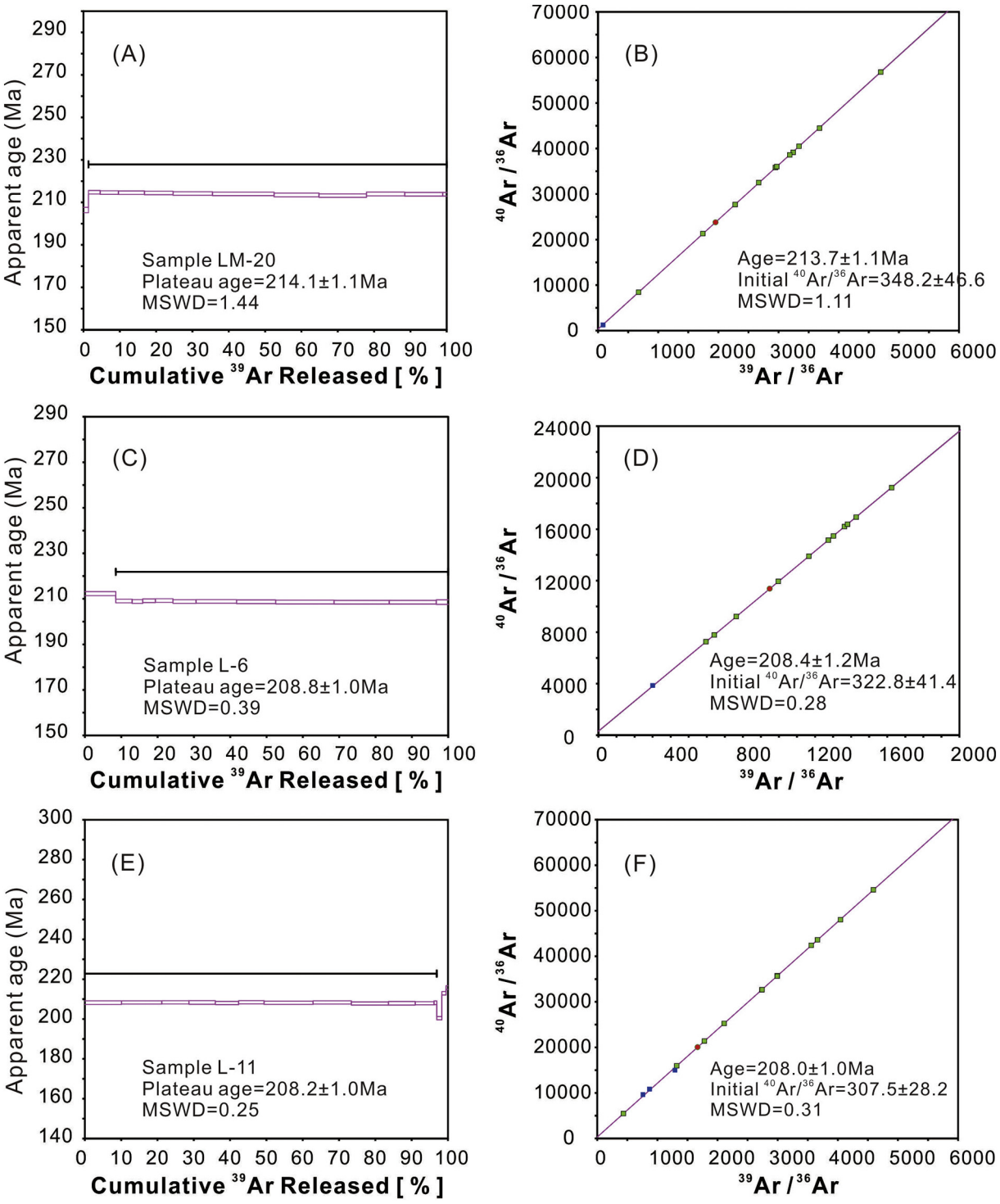

Fig. 7. Apparent muscovite ^{40}Ar/^{39}Ar ages and associated ^{40}Ar/^{36}Ar-^{39}Ar/^{36}Ar isotopic correlation diagrams for representative samples from the Limu ore field.

re-melted at high temperatures during formation of the Indosinian magmas. Such a scenario may well explain the scarce occurrence of the Caledonian zircon in Limu granites (e.g., Ma et al., 2013), and the source of Limu granitic magmas is expected to have contained some melts derived from partial melting of Caledonian granite.

Ta, Nb, Sn, and W are generally strongly incompatible and may be enriched in melts formed by low-degree partial melting or strong fractionation (Linnen et al., 2014; Linnen and Keppler, 1997). The re-melting of Caledonian granite would therefore favor formation of Ta–Nb–Sn–W rich melts and subsequent mineralization, and this may be a reason for Indosinian magmatism in the Limu ore field being associated with large-scale Ta–Nb–Sn–W mineralization.

5.1.2. Fractionation of Limu granitic magmas

The continuous compositional trends of the three granite stages, such as increasing Al_2O_3, Na_2O, Rb, Nb, and Ta contents and decreasing in K_2O, Fe_2O_3, MgO and TiO_2 contents with decreasing ages (Fig. 8), are consistent with the fractional crystallization.

Bulk-rock Zr/Hf and Nb/Ta ratios may be useful indices of the extent of fractional crystallization of felsic melts (Linnen, 1998; Linnen and

Table 2
Major and trace element compositions of the granites in Limu ore field.

Sample	L7	L8	L10	L11	L12	L13	L1	L2	L3	L4	L6	L3–2	L4–2
Rock type	Muscovite granite		Lepidolite granite				Topaz-lepidolite granite						
Major element (wt.%)													
Al_2O_3	13.72	16.35	14.50	14.71	14.32	13.83	16.28	15.87	15.17	15.19	14.59		
CaO	0.04	0.03	0.38	0.38	0.40	0.44	0.13	0.12	0.21	0.15	0.19		
Fe_2O_3	0.94	1.01	1.49	1.24	1.47	1.80	0.39	0.76	0.46	0.47	0.49		
K_2O	3.21	3.57	3.70	4.00	3.99	3.50	3.66	3.73	3.99	3.45	2.90		
MgO	0.22	0.46	0.08	0.07	0.08	0.07	0.05	0.04	0.10	0.04	0.04		
MnO	0.08	0.10	0.10	0.10	0.08	0.10	0.06	0.11	0.14	0.05	0.09		
Na_2O	0.23	0.25	4.15	3.85	3.72	3.68	5.02	5.27	4.86	5.31	4.95		
P_2O_5	0.03	0.02	0.17	0.21	0.19	0.19	0.16	0.20	0.23	0.16	0.20		
SiO_2	78.63	74.54	73.89	74.02	74.34	74.81	73.34	72.98	73.71	74.27	75.69		
TiO_2	0.03	0.03	0.03	0.03	0.03	0.03	0.01	0.01	0.02	0.00	0.01		
L.O·I	2.38	3.27	0.92	0.79	0.78	0.94	0.32	0.29	0.49	0.28	0.23		
Total	99.51	99.63	99.40	99.39	99.40	99.39	99.41	99.38	99.38	99.39	99.39		
ACNK	4.75	5.12	1.57	1.63	1.61	1.63	1.62	1.52	1.49	1.47	1.54		
Sc	2.21	2.31	2.68	2.40	2.17	2.14	0.49	0.51	0.01	0.19	0.08	0.01	0.27
Ti	130	127	137	142	138	155	36.1	64.6	42.4	35.0	44.7	56.0	37.0
V	0.17	0.10	1.03	0.47	0.87	0.72	2.70	1.43	1.05	0.49	0.78	1.22	0.46
Cr	2.35	3.11	3.41	4.15	8.91	3.69	3.58	3.09	2.23	1.37	1.89	3.36	1.52
Mn	762	942	919	947	761	919	575	683	1250	462	804	1084	418
Co	0.47	0.55	0.74	0.63	0.85	0.92	0.46	0.60	0.43	0.41	0.41	0.39	0.41
Ni	1.73	1.53	2.79	1.90	5.76	3.33	1.41	1.86	1.52	1.51	1.55	1.53	1.66
Cu	9.62	11.6	150	8.80	16.2	223	63.3	289	731	89.2	31.2	706	94.0
Zn	18.2	31.9	88.4	75.9	59.9	95.3	19.7	30.0	96.4	28.0	23.5	83.1	27.3
Ga	22.9	31.8	33.8	30.9	28.6	30.7	31.1	23.4	32.4	29.5	28.9	29.4	28.9
Ge	2.66	2.58	2.82	3.71	3.04	2.46	6.25	3.57	5.39	4.75	6.19	6.31	6.97
Rb	1095	1283	1143	1155	1121	1079	1576	657	1494	1215	1086	1361	1194
Sr	7.39	2.42	8.50	6.83	7.69	9.00	7.97	5.82	33.02	5.72	4.03	35.8	6.81
Y	1.28	5.15	11.0	13.0	16.3	14.1	0.17	1.62	0.06	0.16	0.18	0.07	0.18
Zr	28.3	25.0	25.7	23.8	33.4	25.9	23.5	11.5	18.0	17.3	24.6	15.4	17.0
Nb	38.5	40.1	44.1	31.8	24.7	27.4	76.1	37.3	65.5	56.4	71.2	49.6	69.2
Cs	69.2	96.5	51.3	46.6	47.3	43.2	44.3	31.5	34.6	48.6	51.8	34.9	49.8
Ba	47.8	50.1	16.5	2.79	5.00	4.86	4.79	2.24	17.5	2.82	2.99	21.6	3.51
La	2.45	8.28	2.96	3.04	3.70	3.31	0.17	0.32	–	–	–	–	–
Ce	4.89	12.2	7.56	6.16	9.20	8.36	0.30	0.90	–	–	–	–	–
Pr	0.57	2.24	1.03	1.09	1.26	1.19	0.03	0.13	–	–	–	–	–
Nd	1.81	8.34	3.43	3.58	4.37	3.99	0.12	0.47	–	–	–	–	–
Sm	0.40	1.63	1.38	1.60	1.72	1.69	0.02	0.36	–	–	–	–	–
Eu	0.03	0.23	0.01	0.01	0.01	0.01	0.01	0.00	–	–	–	–	–
Gd	0.32	1.24	1.39	1.59	1.86	1.70	0.02	0.29	–	–	–	–	–
Tb	0.06	0.19	0.34	0.42	0.48	0.43	0.00	0.08	–	–	–	–	–
Dy	0.30	0.99	2.02	2.46	2.96	2.51	0.02	0.35	–	–	–	–	–
Ho	0.05	0.17	0.34	0.41	0.50	0.42	0.00	0.04	–	–	–	–	–
Er	0.13	0.46	0.95	1.16	1.42	1.16	0.02	0.10	–	–	–	–	–
Tm	0.03	0.08	0.18	0.21	0.26	0.21	0.00	0.02	–	–	–	–	–
Yb	0.23	0.60	1.39	1.57	1.87	1.56	0.04	0.18	–	–	–	–	–
Lu	0.04	0.09	0.20	0.22	0.26	0.22	0.01	0.02	–	–	–	–	–
Hf	2.60	2.56	2.43	1.90	2.57	2.30	2.84	1.97	2.96	2.72	3.22	2.06	2.17
Ta	20.8	30.1	35.4	10.8	8.3	8.0	93.6	29.0	74.5	46.0	63.8	63.5	55.2
Pb	4.59	1.68	11.3	11.8	13.9	9.23	9.87	16.8	18.6	7.75	6.65	19.0	8.84
Th	7.33	5.40	14.5	11.5	12.2	13.6	5.38	1.99	7.35	6.64	7.28	6.87	9.08
U	2.56	1.83	4.08	22.3	22.0	22.7	8.38	12.35	8.43	8.21	11.2	8.59	8.88
Nb/Ta	1.85	1.33	1.25	2.95	2.96	3.42	0.81	1.29	0.88	1.22	1.12	0.78	1.25
Zr/Hf	10.9	9.8	10.6	12.5	13.0	11.3	8.27	5.85	6.08	6.36	7.63	7.47	7.82
La/Yb_N	7.59	9.92	1.53	1.39	1.42	1.52	3.40	1.26	–	–	–	–	–
Eu_N/Eu^*	0.27	0.50	0.02	0.02	0.02	0.02	0.80	0.04	–	–	–	–	–

Keppler, 1997, 2002; Zaraisky et al., 2008). In the Limu granitic complex, Zr/Hf and Nb/Ta ratios decrease from second- to the third-stage granites (Fig. 8G), suggesting that the late-stage granites are products of highly fractionated melts. The Limu granites have low Nb/Ta ratios (<5), indicating sub-solidus hydrothermal alteration in peraluminous melts (Ballouard et al., 2016) and suggesting that the melts underwent a magmatic-hydrothermal transition during their evolution. The REE tetrad effect fingerprints the interaction between granitic melts and internally derived fluids (Monecke et al., 2002), as observed in second- and third-stages granites but not in the first-stage granites (Fig. 9). The Limu granitic magmas may therefore have achieved volatile saturation after extensive fractionation. Such processes are also recorded in zircons of magmatic origin in first-stage granite (Fig. 5B), whereas those from second- and third-stage magmas exhibit signs of interaction with hydrothermal fluids (Fig. 5C, D).

The most evolved third-stage topaz-lepidolite granite has extremely low bulk-rock REE contents ($\sum$REE < 20 ppm) that are <4% of those of second-stage lepidolite granite (>500 ppm). REEs are mobile in F-rich fluids (Williams-Jones and Migdisov, 2014), and topaz occurs widely in third-stage granite (Fig. 4B, D), so it follows that the late-stage melts were associated with such fluids. This is supported by the zircon trace-element compositions, which show Y/Ho ratios of 53–294 (Appendix 1), substantially higher than the chondritic value of 28 (Anders and Grevesse, 1989). Fractionation of Y and Ho occurs in highly evolved granitic melts with elevated H_2O contents and high Li, B, F, and/or P contents (Bau, 1996). Experimental studies have also demonstrated the

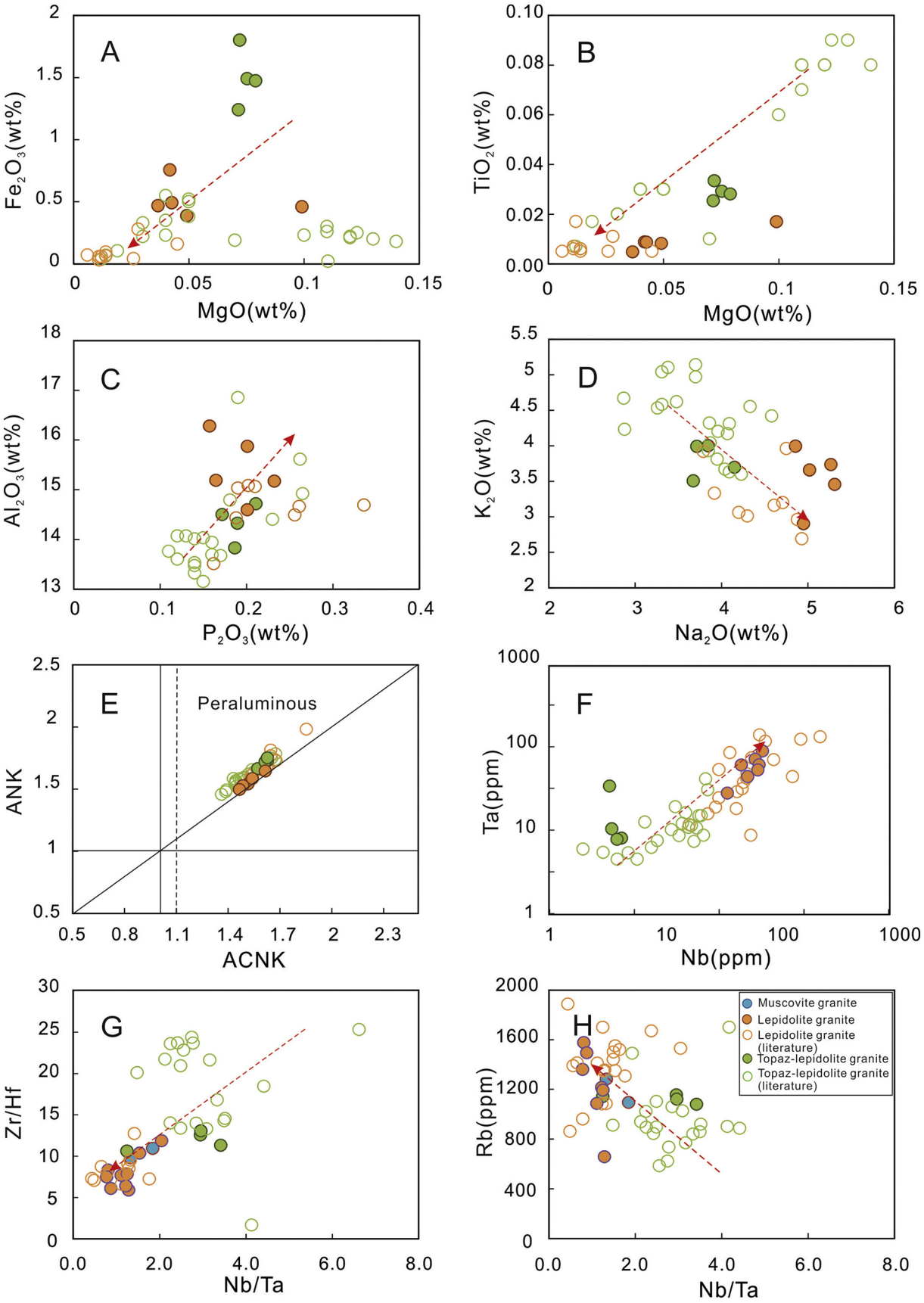

Fig. 8. Plots of (A) Fe_2O_3 versus MgO, (B) TiO_2 versus MgO, (C) Al_2O_3 versus P_2O_3, (D) K_2O versus Na_2O, (E) ANK versus ACNK, (F) Ta versus Nb, (G) Zr/Hf versus Nb/Ta and (H) Rb versus Nb/Ta of the granites in Limu ore field. Open circles represent previously published data (Deng et al., 2012; Dong and Ding, 2016; Wang et al., 2013a, 2013b; Zhang et al., 2013; Zhang et al., 2014).

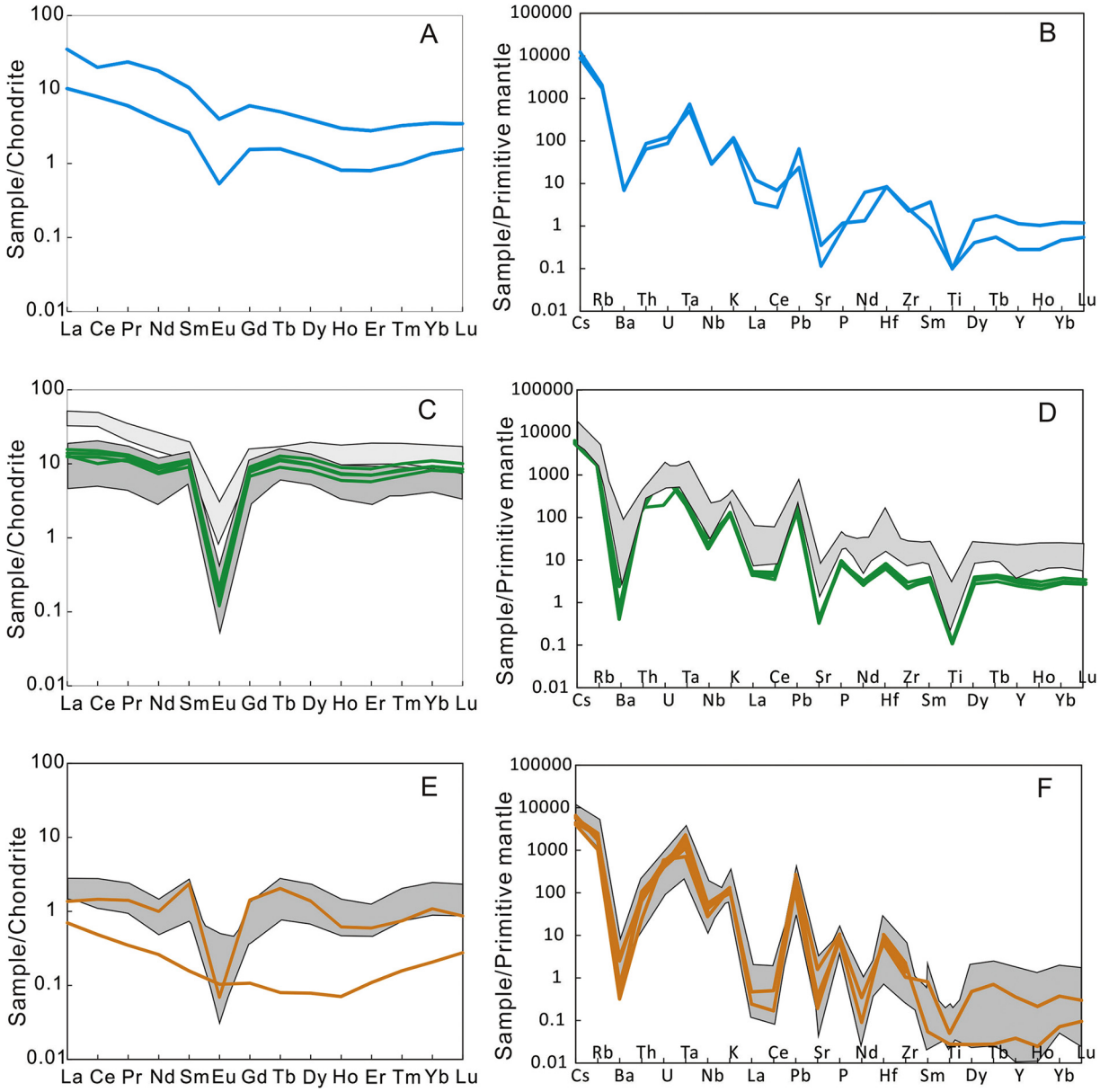

Fig. 9. Chondrite-normalized REE patterns (A, C, E) and primitive-mantle-normalized trace element patterns (B, D, F) for muscovite granite (blue lines), lepidolite granite (green lines), and topaz-lepidolite granite (orange lines). Chondrite and primitive-mantle data are from Sun and McDonough (1989). Gracy-shaded areas indicate ranges of litheraure values (Deng et al., 2012; Dong and Ding, 2016; Wang et al., 2013a, 2013b; Zhang et al., 2013; Zhang et al., 2014).

Table 3
Nd isotopic compositions of the granites in the Limu ore field.

Sample	Age (Ma)	Sm (ppm)	Nd (ppm)	$^{147}Sm/^{144}Nd$	$^{143}Nd/^{144}Nd$	2 σ Err.	$(^{143}Nd/^{144}Nd)_i$	$(^{143}Nd/^{144}Nd)_{CHUR}$	f(Sm/Nd)	ε_{Nd} (0)	ε_{Nd} (t)	$T_{DM,2}$ (Ma)
Muscovite granite												
L7	227	0.399	1.811	0.1332	0.512111	0.000036	0.511920	0.512355	−0.32	−10.27	−8.49	1685
L8	227	1.633	8.342	0.1183	0.512030	0.000022	0.511860	0.512355	−0.40	−11.86	−9.66	1780
Lepidolite granite												
L10	220	1.384	3.428	0.2441	0.512245	0.000006	0.511894	0.512355	0.24	−7.66	−9.00	1726
L12	220	1.724	4.372	0.2384	0.512232	0.000004	0.511889	0.512355	0.21	−7.92	−9.09	1734
L13	220	1.689	3.987	0.2561	0.512256	0.000004	0.511887	0.512355	0.30	−7.46	−9.13	1737

strong influence of F-rich magmatic fluids on Y/Ho ratio of granitic rocks (Veksler et al., 2005). The high Y/Ho ratios of zircons from the evolved Limu granites thus suggest crystallization from late-stage residual melts in the presence of F-rich fluids (Kozlik et al., 2016).

5.2. Timing of mineralization in the Limu ore field

Previous studies have suggested that ore deposits associated with the Limu granite complex were formed during Yanshanian magmatism

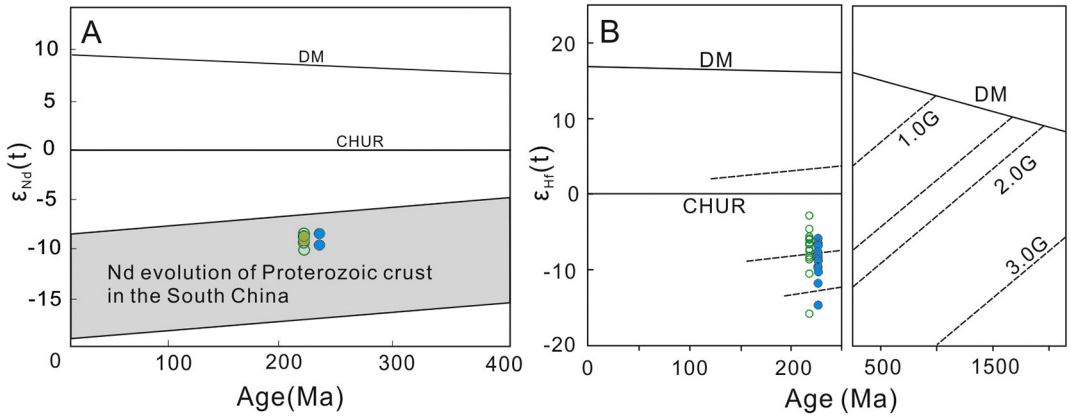

Fig. 10. Plots of (A) bulk-rock εNd(t) values versus U—Pb ages and (B) zircon εHf(t) values versus U—Pb ages for the granites of the Limu ore field. Symbols are the same as in Fig. 8.

in South China (e.g., Lin, 1996;Lin and Wang, 1986 Wang et al., 2008). Recently published zircon U-Pb ages of 230.8 ± 1.1 to 212.3 ± 1.8 Ma and muscovite $^{40}Ar/^{39}Ar$ ages of 205.2 ± 0.7 to 214.1 ± 1.9 Ma (Fig. 11) suggest Indosinian mineralization in the Limu district (Fig. 11). Feng et al. (2019) concluded that the Ta–Nb–Sn–W ores were formed between 224.8 ± 1.6 and 212.3 ± 1.8 Ma, earlier than the quartz-vein W–Sn (type-1) ores (210.0 ± 1.5 to 205.5 ± 1.6 Ma), although that seems inconsistent with other observations. Geological studies have revealed that (1) quartz-vein W-Sn ores (type-1) occur in or around second-stage granite (Li and Pan, 1994; Wang et al., 2008), implying that this mineralization was genetically related to second-stage granite; and (2) Ta–Nb–Sn–W ores, including the quartz-feldspar vein (type-2), pegmatite (type-3), and granite disseminated types (type-4), are closely associated with the third-stage granite (e. g., Zhu et al., 2001; section 2). Ta–Nb–Sn–W ores were therefore formed later than type-1 ores. Furthermore, the ages of type-1 ores of Feng et al. (2019) were constrained by muscovite collected from quartz–feldspar veins, which have a mineral association similar to that of type-2 mineralization.

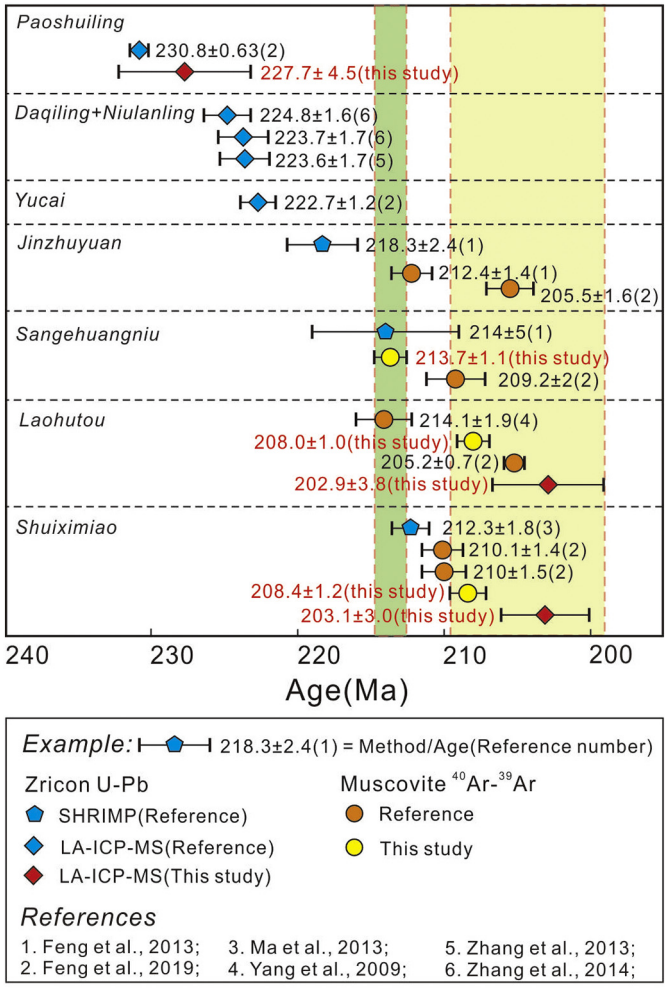

Fig. 11. Summary of published geochronological data for the Limu district.

Our new zircon U–Pb age for first stage muscovite granite from Paoshuiling is 227.7 ± 4.5 Ma, similar to that reported by Feng et al. (2019) and, suggesting that first-stage barren granite was emplaced at ca. 227 Ma (Fig. 11). Our dating of muscovite from type-1 ore hosted in second-stage lepidolite granite (Fig. 3D) yielded an $^{40}Ar/^{39}Ar$ plateau age of 213.7 ± 1.1 Ma, significantly younger than first-stage granite (ca. 227 Ma) and consistent with zircon U–Pb ages of the W–Sn mineralized Sangehuangniu granite (214 ± 5 Ma; Feng et al., 2013) and the muscovite $^{40}Ar/^{39}Ar$ age of greisenized Sn-rich Laohutou granite (214.1 ± 1.9 Ma; Yang et al., 2009). These data indicate that type-1 mineralization formed at ca. 214 Ma, overlapping the ages of second-stage granite (ranging from ca. 225 to ca. 212 Ma). We therefore suggest that type-1 mineralization was genetically associated with second-stage granite.

Type-4 mineralization occurs in third-stage topaz-lepidolite granite (Fig. 3). Zircons from these granites are mostly dark under CL, and have porous and patchy cores overgrowth with thin rims (Fig. 5), suggesting that they were hydrothermally altered (McNaughton et al., 2005). Their geochemical characteristics, such as high Th/U ratios, high Hf contents, slight positive Ce anomalies, and weak depletion of light REEs, are also consistent with those of hydrothermal zircons (Hoskin, 2005; Wang and Ren, 2018). These zircons are similar to those found in other Ta–Nb–Sn–W mineralized granites, such as in the Xianghualing Sn-polymetallic deposit in South China (Li et al., 2018; Wu et al., 2018b) and the Felbertal W–Nb deposit in Austria (Kozlik et al., 2016), which were formed in sub-solvus granitic melt saturated with volatiles. Furthermore, the high Nb and Ta contents of zircons from third-stage topaz-lepidolite granite, especially sample LM-3, indicate that the melts were Nb and Ta rich (Nardi et al., 2012). These zircons may thus have formed coevally with the type-4 mineralization, with apparent U-Pb ages of 202.9 ± 3.8 (MSWD = 4.9) and 203.1 ± 3.0 Ma (MSWD = 5.7) (in Section 4.1), younger than their actual ages on account of Pb loss to hydrothermal fluids (Park et al., 2016; White and Ireland, 2012). These ages thus constrain the lower age limit of type-4 mineralization to no later than ca. 203 Ma. Our $^{40}Ar/^{39}Ar$ plateau ages for two muscovite grains from third-stage topaz-lepidolite granites are 208.0 ± 1.0 and 208.4 ± 1.2 Ma (Section 4.2). As these muscovite grains were co-crystallized with other minerals (Fig. 4B), these ages may record the timing of magmatic emplacement, constraining the

upper age limit of type-4 mineralization in third-stage granite to ca. 208 Ma. The type-4 mineralization may thus have formed at about 208–203 Ma, overlapping the muscovite $^{40}Ar/^{39}Ar$ ages of type-2 (210.1 ± 1.4 to 205.2 ± 1.4 Ma; Feng et al., 2019). The type-2 and type-4 mineralization were thus likely formed coevally, with a genetic association with third-stage granite.

To summarize, our geochronological data indicate that type-1 ores are associated with second-stage granite formed at ca. 214 Ma; and both the type-2 and type-4 mineralization are genetically related to third-stage granites emplaced at ca. 203–208 Ma.

5.3. Genesis of Limu W–Sn and Ta–Nb–Sn–W mineralization

Most rare-metal granites in South China host major W–Sn with relatively little Ta–Nb mineralization, but the Limu granite complex hosts economic deposits of both W–Sn and Ta–Nb–Sn–W. Type-1 mineralization is hosted mainly within second-stage granite or around its contact zones, with its formation involving hydrothermal fluids exsolved from second-stage magma. However, it is not clear whether the Ta–Nb–Sn–W mineralization owes its origin to highly evolved magmas or deuteric fluids (Melcher et al., 2015; Timofeev and Williams-Jones, 2015; Wu et al., 2018a; Zaraisky et al., 2010), with both magmatic (Zhu et al., 2001) and deuteric-fluid (Liang et al., 2017; Wang et al., 2008) origins having been proposed for Ta–Nb–Sn–W deposits in the Limu ore field.

Columbite and tantalite in topaz-lepidolite granite with type-4 mineralization are semi-enclosed by quartz (Fig. 4E), without either alteration or reaction rims between columbite-tantalite and other minerals, suggesting that they crystallized almost simultaneously. As mentioned above (Section 5.1.2), third-stage magmas were volatile-saturated and F-rich. Type-4 was thus of magmatic-hydrothermal origin. Enrichment in volatile elements such as Li, F, and P can substantially increase the solubility of Nb and Ta in the melt (London et al., 1993; Mysen et al., 1981; Xiong et al., 1999), and advanced crystallization of third-stage evolved and volatile-rich granitic melts may therefore be a key factor in large-scale Ta–Nb mineralization.

Cassiterite in topaz-lepidolite granite occurs in the gaps between magmatic K-feldspar and albite (Fig. 4F), with its planar crystal boundaries with these minerals suggesting that they crystallized contemporaneously. Previous studies have indicated that fractional crystallization of per-aluminous melts may enrich residual melts with Sn up to 0.7 wt.% (Duc-Tin et al., 2007; Thomas et al., 2006; Thomas and Webster, 2000). Therefore, Sn may also be extracted and transported by H_2O-saturated, per-aluminous, F- and B- bearing melts. The third-stage granitic magma was H_2O-saturated and co-existed with F-rich fluid. It follows that Sn (W) mineralization co-genetic with disseminated Ta–Nb mineralization may be attributed to advanced crystallization of evolved melts.

The Limu type-2 and type-3 mineralization may have been formed through post-magmatic hydrothermal processes (Feng et al., 2019). Here, we observed that these mineralization types have Ta_2O_5/Nb_2O_5 and WO_3/Sn ratios (1.36 and 0.08, respectively) similar to those of magmatic-hydrothermal type-4 mineralization (Ta_2O_5/Nb_2O_5 = 0.89 to 1.24; WO_3/Sn = <0.01–0.13, Table 1) and distinct from those of type-1 mineralization, which has a higher WO_3/Sn ratio of ~1.40 and low Nb–Ta contents (Li and Pan, 1994;Wang et al., 2008; Table 1).

Ta, Nb, W and Sn are usually incompatible during magma evolution (Linnen and Keppler, 1997) but the hydrothermal behaviors of Ta and Nb are different from those of W and Sn. Nb and Ta have very low fluid-melt partition coefficients ($D_{Ta}^{fluid/melt}$ = 0.002–0.08; $D_{Nb}^{fluid/melt}$ = 0.005–0.08; Chevychelov et al., 2005), whereas W and Sn tend to enter the fluid phase with partition coefficients of 0.8–60 and 0.3–42, respectively (Keppler and Wyllie, 1991; Zajacz et al., 2008). It follows that W–Sn mineralization derived from deuteric fluid has higher WO_3/Sn ratios than that derived from magma, with the fluid-melt partition coefficient of W being higher than that of Sn in the haplogranite–H_2O–F system (Keppler and Wyllie, 1991). This diversity of WO_3/Sn ratios between type-1 and type-2 mineralization suggests that these mineralization types were not co-genetic. We conclude that type-2 and type-3 mineralization have origins similar to that of type-4 mineralization, with all being of magmatic-hydrothermal origin.

To summarize, Limu W–Sn and Ta–Nb–Sn–W mineralization formed through different processes, with W-Sn (type-1) mineralization being controlled by strong fractionation of granite and associated fluid exsolution, and Ta–Nb–Sn–W mineralization (type-2, type-3, and type-4) being of magmatic-hydrothermal origin with advanced crystallization of evolved and volatile-rich granitic melt.

5.4. Geodynamic setting for the formation of the Limu granite complex

Geochronological data indicate that magma chamber survived for over 15 Myr in the Limu district (Fig. 11), which is similar to the duration (10 Myr) of Sn mineralization related to the Harney Peak granite–pegmatite at Black Hill, South Dakota, USA (Krogstad and Walker, 1994). The long-lived magma chamber owed its origin to the continuous supply of heat and the low-temperature solidus, which were enhanced by additional heat transferred from a deep source and the increasing flux component during fractional crystallization, respectively (Manning, 1981; Webster et al., 2004).

The formation of the Limu Indosinian granite complex has previously been considered to have been triggered by intra-continental orogenic events (Zhang et al., 2014), including far-field stresses of collision between the Indochina and South China blocks and between the North China and South China blocks (e.g., Chen, 1999; Gao et al., 2017; Ren et al., 2018), with the Indosinian events lead to crust thickening and the Triassic magmatism (Huang et al., 2017b; Wang et al., 2013a, 2013b; Wu et al., 2012). However, internal heating of thickened crust may eventually result in minimum-temperature melting (Clark et al., 2011), forming low-temperature melts and related Li–Ce–Ta mineralization (Romer and Kroner, 2016). Such conditions were unlikely in the Limu district, where granitic melts were rich in W, Sn, Ta and Nb. To form such melts, high-temperature anatexis would have been required, as Sn is mainly hosted in magnetite, biotite, rutile, titanite, and ilmenite (Brenan et al., 1995; Linnen and Keppler, 1997; Stepanov et al., 2014). High-temperature crustal anatexis is usually driven by advective mantle heat (Castro, 2014; Romer and Kroner, 2016). Liang et al. (2013) determined that revealed that 2.2%–15.9% of noble gas in ore-forming fluids of the Limu deposit was derived from the mantle, with $^3He/^4He$ ratios of 0.14–0.97 Ra, suggesting that mantle heat was involved in the formation of Limu granitic melts. The Limu ore field in the lithospheric Guangyingge-Zhuhou fault zone, which could have provided a channel for heat transfer from the mantle during asthenospheric upwelling.

The Indosinian Orogeny caused crustal thickening in South China (Huang et al., 2017b; Wang et al., 2013a, 2013b; Wu et al., 2012) through which the underlying lithospheric mantle may have undergone eclogitic metamorphism, forming a high-density eclogitic root in the lower lithospheric mantle. High-density eclogitic metamorphic rock

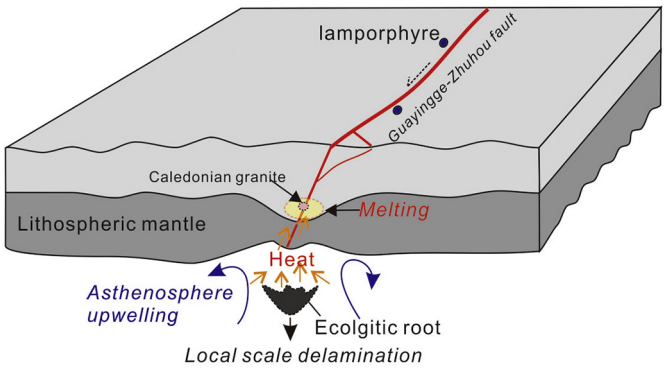

Fig. 12. Sketch model of the generation of magmas in the Limu ore field.

could have detached from the lithosphere and sunk to the asthenosphere on account of to its high density, inducing asthenospheric upwelling. There is no large scale Indosinian mafic or felsic magmatism in South China, so any lithospheric thinning and asthenospheric upwelling may have been local (Drew et al., 2009). This limited upwelling could have supplied heat through the Guanyingge-Zhuhou fault zone for high-temperature anatexis and formation of the Limu granite complex. Such processes would have favored high-temperature partial melting and formation of the long-lived magma chamber that ultimately gave rise to highly evolved and Ta–Nb–Sn–W rich melts in the Limu ore field (Fig. 12).

6. Conclusions

(1) Limu granitic magmas were derived from Proterozoic basement with a contribution of re-melted Caledonian granite.
(2) Quartz-vein W–Sn mineralization associated with second-stage granite formed at ca. 214 Ma, with a deuteric hydrothermal origin.
(3) Ta–Nb–Sn–W mineralization was formed simultaneously with third-stage granite (at 208–203 Ma), via advanced crystallization of volatile-rich, evolved granitic melt.
(4) The formation of long-lasting, evolved, and Ta–Nb–Sn–W rich magmas in the Limu ore field was driven by continuous heating from the mantle as a result of local scale delamination, asthenospheric upwelling, and deep fault activity.

Declaration of Competing Interest

None.

Acknowledgments

Staff of the Limu mining company are thanked for their help during field work. This work was supported by the Natural Science Foundation of China (41772065) and the National Key R & D Program of China (No. 2016YFC0600407). We appreciate the constructive review by Yigang Xu and comments from two anonymous reviewers. This is contribution No. IS-2786 from GIGCAS.

Appendix A. Supplementary data

Supplementary data to this article can be found online at https://doi.org/10.1016/j.lithos.2019.105321.

References

Anders, E., Grevesse, N., 1989. Abundances of the elements - meteoritic and solar. Geochim. Cosmochim. Acta 53 (1), 197–214.
Ballouard, C., Branquet, Y., Tartese, R., Poujol, M., Boulvais, P., Vigneresse, J.L., 2016. Nb-Ta fractionation in peraluminous granites: a marker of the magmatic-hydrothermal transition. Geology 44 (7), 231–234.
Bau, M., 1996. Controls on the fractionation of isovalent trace elements in magmatic and aqueous systems: evidence from Y/Ho: Zr/Hf, and lanthanide tetrad effect. Contrib. Miner. Petrol. 123 (3), 323–333.
Black, L.P., Kamo, S.L., Allen, C.M., Aleinikoff, J.N., Davis, D.W., Korsch, R.J., Foudoulis, C., 2003. TEMORA 1: a new zircon standard for phanerozoic U–Pb geochronology. Chem. Geol. 200 (1–2), 155–170.
Brenan, J.M., Shaw, H.F., Ryerson, F.J., Phinney, D.L., 1995. Mineral-aqueous fluid partitioning of trace-elements at 900-degrees-C and 2.0: Gpa - constraints on the trace-element chemistry of mantle and deep-crustal fluids. Geochim. Cosmochim. Acta 59 (16), 3331–3350.
Castro, A., 2014. The off-crust origin of granite batholiths. Geosci. Front. 5 (1), 63–75.
Chen, A., 1999. Mirror-image thrusting in the South China orogenic belt: tectonic evidence from western Fujian, southeastern China. Tectonophysics 305 (4), 497–519.
Chen, J.Y., Lu, J.J., Chen, W.F., Wang, R.C., Ma, D.S., Zhu, J.C., Zhang, W.L., Ji, F.F., 2008. W-Sn-Nb-Ta-bearing granites in the Nanling Range and their relationship to metallogengesis. Geol. J. China Univ. 14 (4), 45–473.
Chen, X., Liang, H., Richards, J.P., Huang, W., Zhang, J., Wu, J., Sotiriou, P., 2018. Age and granite association of skarn W mineralization at Niutangjie district, South China Block. Ore Geol. Rev. 102, 268–283.
Chevychelov, V.Y., Zaraisky, G.P., Borisovskii, S.E., Borkov, D.A., 2005. Effect of melt composition and temperature on the partitioning of Ta, Nb, Mn, and F between granitic (alkaline) melt and fluorine-bearing aqueous fluid: fractionation of Ta and Nb and conditions of ore formation in rare-metal granites. Petrology 13 (4), 305–321.
Clark, C., Fitzsimons, I.C.W., Healy, D., Harley, S.L., 2011. How does the continental crust get really hot? Elements 7 (4), 235–240.
Deng, G., Wu, J., Wang, S., Desong, Linm, 2012. Geological characteristics of Sanggehuangniu granite-type tungsten-tin deposit in the Limu ore field. Miner. Resour. Geol. 26, 1–6.
Dong, Y., Ding, R., 2016. Restraint factors of geochemical characteristics and dynamic backgroud of granite bodies in Limu ore field of Guangxi. Miner. Resour. Geol. 30, 998–1005.
Drew, S.T., Ducea, M.N., Schoenbohm, L.M., 2009. Mafic volcanism on the Puna Plateau, NW Argentina: implications for lithospheric composition and evolution with an emphasis on lithospheric foundering. Lithosphere 1 (5), 305–318.
Duc-Tin, Q., Audetat, A., Keppler, H., 2007. Solubility of tin in (Cl, F)-bearing aqueous fluids at 700 degrees C, 140 MPa: A LA-ICP-MS study on synthetic fluid inclusions. Geochim. Cosmochim. Acta 71 (13), 3323–3335.
Feng, Z., Kang, Z., Yang, F., Liao, J., Wang, C., 2013. Geochronology of the Limu W-Sn-Nb-Ta-Bearing Granite Pluton in South China. Resour. Geol. 63 (3), 320–329.
Feng, M., Feng, Z., Kang, Z., Fu, W., Qing, Y., Hu, R., Cai, Y., Feng, Y., Wang, C., 2019. Establishing an Indosinian geochronological framework for episodic granitic emplacement and W-Sn-Nb-Ta mineralization in Limu mining district, South China. Ore Geol. Rev. 107, 1–13.
Gao, P., Zheng, Y.F., Zhao, Z.F., 2017. Triassic granites in South China: a geochemical perspective on their characteristics, petrogenesis, and tectonic significance. Earth-Sci. Rev. 173, 266–294.
Guo, C.L., Chen, Y.C., Zeng, Z.L., Lou, F.S., 2012. Petrogenesis of the Xihuashan granites in southeastern China: constraints from geochemistry and in-situ analyses of zircon U-Pb-Hf-O isotopes. Lithos 148, 209–227.
GXGBMR (Bureau of Geology and Mineral Resources of Guangxi Province), 1985. Reginal Geology of the Guangxi Province. Geological Publishing House, Beijing, China, p. 350 (in Chinese with English summary).
Hoskin, P.W.O., 2005. Trace-element composition of hydrothermal zircon and the alteration of Hadean zircon from the Jack Hills, Australia. Geochim. Cosmochim. Acta 69 (3), 637–648.
Huang, W.T., Liang, H.Y., Wu, J., Zou, Y.Q., Zhang, J., 2017a. Formation of porphyry Mo deposit in a deep fault zone, example from the Dabaoshan porphyry Mo deposit in northern Guangdong, South China. Ore Geol. Rev. 81, 940–952.
Huang, W.T., Wu, J., Zhang, J., Liang, H.Y., Qiu, X.L., 2017b. Geochemistry and Hf-Nd isotope characteristics and forming processes of the Yuntoujie granites associated with W-Mo deposit, Guangxi, South China. Ore Geol. Rev. 81, 953–964.
Huang, W., Liang, H., Wu, L., Wu, J., Li, J., Bao, Z., 2018. Asynchronous formation of the adjacent epithermal Au-Cu and porphyry Cu-Mo deposits in the Zijinshan orefield, Southeast China. Ore Geol. Rev. 102, 351–367.
Jochum, K.P., Weis, U., Stoll, B., Kuzmin, D., Yang, Q.C., Raczek, I., Jacob, D.E., Stracke, A., Birbaum, K., Frick, D.A., Gunther, D., Enzweiler, J., 2011. Determination of reference values for NIST SRM 610–617 glasses following ISO guidelines. Geostand. Geoanal. Res. 35 (4), 397–429.
Keppler, H., Wyllie, P.J., 1991. Partitioning of Cu, Sn, Mo, W, U, and Th between melt and aqueous fluid in the systems haplogranite-H_2O HCl and haplogranite-H_2O Hf. Contrib. Miner. Petrol. 109 (2), 139–150.
Koppers, A.A., 2002. ArArCALC-software for $^{40}Ar/^{39}Ar$ age calculations. Comput. Geosci. 28, 605–619.
Kozlik, M., Raith, J.G., Gerdes, A., 2016. U-Pb, Lu-Hf and trace element characteristics of zircon from the Felbertal scheelite deposit (Austria): new constraints on timing and source of W mineralization. Chem. Geol. 421, 112–126.
Krogstad, E.J., Walker, R.J., 1994. High Closure Temperatures of the U-Pb System in large Apatites from the Tin Mountain Pegmatite, Black-Hills, South-Dakota, USA. Geochim. Cosmochim. Acta 58 (18), 3845–3853.
Li, Z.X., Li, X.H., 2007. Formation of the 1300-km-wide intracontinental orogen and postorogenic magmatic province in Mesozoic South China: a flat-slab subduction model. Geology 35 (2), 179–182.
Li, X.-H., Long, W.-G., Li, Q.-L., Liu, Y., Zheng, Y.-F., Yang, Y., Chamberlain, K.R., Wan, D.-F., Guo, C.-H., Wang, X.-C., Tao, H., 2010. Penglai Zircon Megacrysts: A Potential New Working Reference Material for Microbeam Determination of Hf–O Isotopes and U–Pb Age. Geostandards and Geoanalytical Research 34 (2), 117–134.
Li, R.K., Pan, Q.Y., 1994. Discoery history of Limu W-Sn rare metal min in Gongcheng county of Guangxi. Guangxi Geol. 7, 85–88.
Li, X.H., Li, Z.X., Li, W.X., Liu, Y., Yuan, C., Wei, G.J., Qi, C.S., 2007. U-Pb zircon, geochemical and Sr-Nd-Hf isotopic constraints on age and origin of Jurassic I- and A-type granites from central Guangdong, SE China: a major igneous event in response to foundering of a subducted flat-slab? Lithos 96 (1–2), 186–204.
Li, J., Huang, X.L., He, P.L., Li, W.X., Yu, Y., Chen, L.L., 2015a. In situ analyses of micas in the Yashan granite, South China: constraints on magmatic and hydrothermal evolutions of W and Ta-Nb bearing granites. Ore Geol. Rev. 65, 793–810.
Li, W., Bi, S.J., Yang, Z., Liang, P., Tang, K.F., 2015b. Zircon U-Pb age and Hf isotope characterization of Sheshan Granodiorite in Southern edge of Dayaoshan: Guidong: consteaints on Caledonian Diagenesis and mineralization. Earth Sci. J. China Univ. Geosci. 40 (1), 17–33.
Li, H., Wu, J.H., Evans, N.J., Jiang, W.C., Zhou, Z.K., 2018. Zircon geochronology and geochemistry of the Xianghualing A-type granitic rocks: insights into multi-stage Sn-polymetallic mineralization in South China. Lithos 312, 1–20.
Liang, X.R., Wei, G.J., Li, X.H., Liu, Y., 2003. Precisemeasurement of 143Nd/144Nd and Sm/Nd ratios using multiple-collectors inductively coupled plasma-mass spectrometer (MCICPMS). Geochimica 32, 91–96.

Liang, H.Y., Campbell, I.H., Allen, C., Sun, W.-D., Liu, C.-Q., Yu, H.-X., Xie, Y.-W., Zhang, Y.Q., 2006. Zircon Ce^{4+}/Ce^{3+} ratios and ages for Yulong ore-bearing porphyries in eastern Tibet. Miner. Dep. 41 (2), 152–159.
Liang, L.H., Peng, Z.A., Wang, M., K, N., Cai, M.H., J, H.D., Guo, T.F., Liu, H., Cheng, L., 2013. Noble gas isotopic tracing of ore-forming fluids in Limu tin-niobium-tantalum deposit. Miner. Dep. 32 (2), 397–404.
Liang, L., Zhang, L., G., Y. Z., and C., D. Y., 2017. Liquid-gas fractionation and mineralization in the Limu granites, Guangxi. Geol. Rev. 63 (1), 61–72.
Lin, D.S., 1996. Tantalum-Rich Type Granite Deposits in South China. Geological Publishing House, Beijing, pp. 1–147.
Lin, D.S., Wang, K.X., 1986. Study on surface indication zone of granite type Sn-Ta-Nb deposit (take Limu ore area for an example). Miner. Resour. Geol. (1), 10–18.
Linnen, R.L., 1998. The solubility of Nb-Ta-Zr-Hf-W in granitic melts with Li and Li+F: Constraints for mineralization in rare metal granites and pegmatites. Econ. Geol. Bull. Soc. Econ. Geol. 93 (7), 1013–1025.
Linnen, R.L., Keppler, H., 1997. Columbite solubility in granitic melts: consequences for the enrichment and fractionation of Nb and Ta in the Earth's crust. Contrib. Miner. Petrol. 128 (2–3), 213–227.
Linnen, R.L., Keppler, H., 2002. Melt composition control of Zr/Hf fractionation in magmatic processes. Geochim. Cosmochim. Acta 66 (18), 3293–3301.
Linnen, R.L., Samson, I.M., Williamsjones, A.E., Chakhmouradian, A.R., 2014. Geochemistry of the Rare-Earth Element, Nb, Ta, Hf, and Zr Deposits. 2nd ed. Treatise on GeochemistryElsevier, Oxford.
Liu, Y., Liu, H.C., Li, X.H., 1996. Simultaneous and precise determination of 40 trace elements in rock samples using ICP-MS. Geochimica 25, 552–558.
Liu, Y.S., Hu, Z.C., Zong, K.Q., Gao, C.G., Gao, S., Xu, J.A., Chen, H.H., 2010. Reappraisement and refinement of zircon U-Pb isotope and trace element analyses by LA-ICP-MS. Chin. Sci. Bull. 55 (15), 1535–1546.
Liu, X., Zhou, F.C., B., H. Z., Li, J. K., Zhou, H. X., Xiao, G. Q., Bao, Y. H., Wang, X. M., Lin, Y., and Liu, X. M., 2018. Discovery of Renli superlarge pegmatite-type Nb-Ta polymetallic deposit in Pingjiang, Hunan province and its significances. Geotect. Metall. 42 (2), 335–342.
London, D., Morgan, G.B., Babb, H.A., Loomis, J.L., 1993. Behavior and effects of phosphorus in the system Na_2O-K_2O-Al_2O_3-SiO_2-P_2O_5-H_2O at 200 Mpa (H_2O). Contrib. Miner. Petrol. 113 (4), 450–465.
Ludwig, K.R., 2003. User's Manual for Isoplot 3.00: A Geochronological Toolkit for Microsoft Excel. 4. Kenneth R. Ludwig.
Ma, L.Y., Fu, J.M., Cheng, S.B., Lu, Y.Y., Xu, D.M., Chen, X.Q., 2013. SHRIMP U-Pb zircon dating and its significance of mineralized granite in Limu Sn-Nb-Ta ore field, Guangxi, South China. Geol. Miner. Resour. South China 29 (4), 292–298.
Manning, D.A.C., 1981. The Effect of fluorine on liquidus phase-relationships in the system Qz-Ab-or with excess water at 1-Kb. Contrib. Mineral. Petrol. 76 (2), 206–215.
Mao, J.W., Xie, G.Q., Guo, C.L., Chen, Y.C., 2007. Large-scale tungsten-tin mineralization in the Nanling region, South China: metallogenic ages and corresponding geodynamic processes. Acta Petrol. Sin. 23 (10), 2329–2338.
Mao, J.W., Pirajno, F., Cook, N., 2011. Mesozoic metallogeny in East China and corresponding geodynamic settings - an introduction to the special issue. Ore Geol. Rev. 43 (1), 1–7.
McNaughton, N.J., Mueller, A.G., Groves, D.I., 2005. The age of the giant Golden Mile deposit, Kalgoorlie, Western Australia: Ion-microprobe zircon and monazite U-Pb geochronology of a synmineralization lamprophyre dike. Econ. Geol. 100 (7), 1427–1440.
Melcher, F., Graupner, T., Gabler, H.E., Sitnikova, M., Henjes-Kunst, F., Oberthur, T., Gerdes, A., Dewaele, S., 2015. Tantalum-(niobium-tin) mineralisation in African pegmatites and rare metal granites: constraints from Ta-Nb oxide mineralogy, geochemistry and U-Pb geochronology. Ore Geol. Rev. 64, 667–719.
Monecke, T., Kempe, U., Monecke, J., Sala, M., Wolf, D., 2002. Tetrad effect in rare earth element distribution patterns: a method of quantification with application to rock and mineral samples from granite-related rare metal deposits. Geochim. Cosmochim. Acta 66 (7), 1185–1196.
Mysen, B.O., Ryerson, F.J., Virgo, D., 1981. The Structural role of phosphorus in silicate melts. Am. Miner. 66 (1–2), 106–117.
Nardi, L.V.S., Formoso, M.L.L., Jarvis, K., Oliveira, L., Neto, A.C.B., Fontana, E., 2012. REE, Y, Nb, U, and Th contents and tetrad effect in zircon from a magmatic-hydrothermal F-rich system of Sn-rare metal-cryolite mineralized granites from the Pitinga Mine, Amazonia, Brazil. J. S. Am. Earth Sci. 33 (1), 34–42.
Park, C., Song, Y., Chung, D., Kang, I.M., Khulganakhuu, C., Yi, K., 2016. Recrystallization and hydrothermal growth of high U-Th zircon in the Weondong deposit, Korea: record of post-magmatic alteration. Lithos 260, 268–285.
Pearce, N.J.G., Perkins, W.T., Westgate, J.A., Gorton, M.P., Jackson, S.E., Neal, C.R., Chenery, S.P., 1997. A compilation of new and published major and trace element data for NIST SRM 610 and NIST SRM 612 glass reference materials. Geostand. Newsl. J. Geostand. Geoanal. 21 (1), 115–144.
Qiu, H.N., Wijbrans, J.R., 2006. When did amphibolite-facies overprinting occur in Dabieshan? Geochim. Cosmochim. Acta 70 (18), A512.
Ren, L., Liang, H., Bao, Z., Zhang, J., Li, K., Huang, W., 2018. Genesis of the high Sr/Y rocks in Qinling orogenic belt, Central China. Lithos 314–315, 337–349.
Renne, P.R., Cassata, W.S., Morgan, L.E., 2009. The isotopic composition of atmospheric argon and Ar-40/Ar-39 geochronology: time for a change? Q. Geochronol. 4 (4), 288–298.
Romer, R.L., Kroner, U., 2016. Phanerozoic tin and tungsten mineralization-Tectonic controls on the distribution of enriched protoliths and heat sources for crustal melting. Gondw. Res. 31, 60–95.
Sang, H.Q., Wang, F., He, H.Y., Wang, Y.L., Yang, L.K., Zhu, R.X., 2006. Intercalibration of ZBH-25 biotite reference material untilized for K-Ar and ^{40}Ar-^{39}Ar age determination. Acta Petrol. Sin. 22 (12), 3059–3078.
Shu, L.S., Faure, M., Wang, B., Zhou, X.L., Song, B., 2008. Late palaeozoic-early mesozoic geological features of South China: response to the Indosinian collision events in Southeast Asia. Compt. Rend. Geosci. 340 (2–3), 151–165.
Stepanov, A., Mavrogenes, J.A., Meffre, S., Davidson, P., 2014. The key role of mica during igneous concentration of tantalum. Contrib. Miner. Petrol. 167 (6).
Sun, T., 2006. A new map showing the distribution of granites in South China and its explanatory notes. Geol. Bull. China 25 (3), 332–335.
Sun, S.S., McDonough, W.F., 1989. Chemical and isotopic systematics of oceanic basalts: Implication for mantle composition and processes. In: Saunder, A.D., Norry, M.J. (Eds.), Magmatism in the Ocean Basins. Geological Society Special Publication 42, pp. 313–345.
Thomas, R., Webster, J.D., 2000. Strong tin enrichment in a pegmatite-forming melt. Miner. Deposita 35 (6), 570–582.
Thomas, R., Webster, J.D., Rhede, D., Seifert, W., Rickers, K., Forster, H.J., Heinrich, W., Davidson, P., 2006. The transition from peraluminous to peralkaline granitic melts: evidence from melt inclusions and accessory minerals. Lithos 91 (1–4), 137–149.
Timofeev, A., Williams-Jones, A.E., 2015. The origin of niobium and tantalum mineralization in the nechalacho REE Deposit, NWT, Canada. Econ. Geol. 110 (7), 1719–1735.
Tu, X.L., Zhang, H., Deng, W.F., Ling, M.X., Ying, L.H., Liu, Y., Sun, W.D., 2011. Application of resolution in-situ laser ablation ICP-MS in trace element analyses. Geochimica 40 (1), 83–98.
Veksler, I.V., Dorfman, A.M., Kamenetsky, M., Dulski, P., Dingwell, D.B., 2005. Partitioning of lanthanides and Y between immiscible silicate and fluoride melts, fluorite and cryolite and the origin of the lanthanide tetrad effect in igneous rocks. Geochim. Cosmochim. Acta 69 (11), 2847–2860.
Wang, X., Ren, M.H., 2018. Constraints of hydrothermal and magmatic zircon on the origin of the Yaogangxian tungsten deposit, southern China. Ore Geol. Rev. 101, 453–467.
Wang, Y.J., Fan, W.M., Zhang, G.W., Zhang, Y.H., 2013a. Phanerozoic tectonics of the South China Block: Key observations and controversies. Gondwana Res. 23 (4), 1273–1305.
Wang, Y., Peng, Q., Zhu, X., Fu, Q., Yang, L., 2013b. Liquid immiscibility of granitic magma and its relationship with the mineralization in the Limu Sn-W-Nb-Ta ore deposit, Guangxi Province. Geol. Explor. 49, 1046–1055.
Wang, S.S., Zhang, Q.Z., Tang, Z.G., Wang, L., 2008. The geological characteristics and factors controlling the mineralization of the Limu ganite type Sn-Nb-Ta deposit in Guangxi. Da Zhong Ke Ji 11, 111–112 (in Chinese).
Webster, J., Thomas, R., Forster, H.J., Seltmann, R., Tappen, C., 2004. Geochemical evolution of halogen-enriched granite magmas and mineralizing fluids of the Zinnwald tin-tungsten mining district, Erzgebirge, Germany. Miner. Dep. 39 (4), 452–472.
Wei, G.J., Liang, X.R., Li, X.H., Liu, Y., 2002. Precisemeasurement of Sr isotopic composition of liquid and solid base using (LP) MC-ICPMS. Geochimica 31, 295–299.
White, L.T., Ireland, T.R., 2012. High-uranium matrix effect in zircon and its implications for SHRIMP U-Pb age determinations. Chem. Geol. 306, 78–91.
Williams-Jones, A.E., Migdisov, A.A., 2014. Experimental Constraints on the Transport and Deposition of Metals in Ore-Forming Hydrothermal Systems: Building Exploration Capability for the 21st Century. 18 pp. 77–95.
Wu, F.-Y., Yang, Y.-H., Xie, L.-W., Yang, J.-H., Xu, P., 2006. Hf isotopic compositions of the standard zircons and baddeleyites used in U–Pb geochronology. Chem. Geol. 234 (1), 105–126.
Wu, J., Liang, H.Y., Huang, W.T., Wang, C.L., Sun, W.D., Sun, Y.L., Li, J., Mo, J.H., Wang, X.Z., 2012. Indosinian isotope ages of plutons and deposits in southwestern Miaoershan-Yuechengling, northeastern Guangxi and implications on Indosinian mineralization in South China. Chin. Sci. Bull. 57 (9), 1024–1035.
Wu, M.Q., Samson, I.M., Zhang, D.H., 2017. Textural and chemical constraints on the formation of disseminated granite-hosted W-Ta-Nb mineralization at the dajishan deposit, nanling range, Southeastern China. Econ. Geol. 112 (4), 855–887.
Wu, J.H., Li, H., Algeo, T.J., Jiang, W.C., Zhou, Z.K., 2018a. Textural features and chemical evolution in Ta-Nb oxides: implications for deuteric rare-metal mineralization in the yichun granite-marginal pegmatite, Southeastern China. Econ. Geol. 113 (4), 937–960.
Wu, M.Q., Samson, I.M., Zhang, D.H., 2018b. Genesis of the Xianghualing Sn-Pb-Zn deposit, South China: a multi-method zircon study. Ore Geol. Rev. 102, 220–239.
Xie, L., Wang, Z.J., Wang, R.C., Zhu, J.C., Che, X.D., Gao, J.F., Zhao, X., 2018. Mineralogical constraints on the genesis of W-Nb-Ta mineralization in the Laiziling granite (Xianghualing district, South China). Ore Geol. Rev. 95, 695–712.
Xiong, X.L., Zhao, Z.H., Zhu, J.C., Rao, B., 1999. Phase relations in albite granite-H2O-HF system and their petrogenetic application. Geochem. J. 33 (3), 199–214.
Xu, D., Fu, J., Chen, X., Cheng, S., Ma, L., Zhang, K., Huang, H., 2017. Formation age and petrogenesis of the dupangling rapakivi granites and its geological significance. Geotect. Metall. 41, 561–576.
Yang, F., Li, X.F., Feng, Z.H., Bai, Y.P., 2009. 40Ar-39Ar dating of muscovite from greisenized granite and geological significance in Limu tin deposit. J. Guilin Univ. Technol. 2, 21–24.
Zajacz, Z., Halter, W.E., Pettke, T., Guillong, M., 2008. Determination of fluid/melt partition coefficients by LA-ICPMS analysis of co-existing fluid and silicate melt inclusions: controls on element partitioning. Geochim. Cosmochim. Acta 72 (8), 2169–2197.
Zaraisky, G., Aksyuk, A., Devyatova, V., Udoratina, O., Chevychelov, V., 2008. Zr/Hf ratio as an indicator of fractionation of rare-metal granites by the example of the Kukulbei complex, eastern Transbaikalia. Petrology 16 (7), 710–736.
Zaraisky, G.P., Korzhinskaya, V., Kotova, N., 2010. Experimental studies of Ta2O5 and columbite-tantalite solubility in fluoride solutions from 300 to 550A degrees C and 50 to 100 MPa. Miner. Petrol. 99 (3–4), 287–300.
Zhang, L., Ren, Z.-Y., Xia, X.-P., Li, J., Zhang, Z.-F., 2015. IsotopeMaker: A Matlab program for isotopic data reduction. International Journal of Mass Spectrometry 392, 118–124.
Zhang, W.L., Wang, R.C., Hua, R.M., 2006. Study of a series of Ta-minerals in Dajishan W-Nb-Ta deposit, south China. Geochim. Cosmochim. Acta 70 (18), A739.

Zhang, H., Lu, J., Wang, R., Zhang, R., 2013. Confirmation of indosinian age of the niulanling granite from limu orefield, Guangxi Province and its significance geological. J. China Univ. 19, 220–232.

Zhang, H., Lu, J., Wang, R., Ma, D., Zhu, J., Zhang, R., 2014. Petrogenesis of the concealed Daqiling intrusion in Guangxi and its tectonic significance: constraints from geochemistry, zircon U-Pb dating and Nd-Hf isotopic compositions. Sci. China Earth Sci. 57 (8), 1723–1740.

Zhou, Z.H., Che, H.W., Ma, X.H., Gao, X., 2016. Magmatic evolution and mineralization process of the super-large shihuiyao Rb-Nb-Ta deposit, Southern Great Xing'an Range, China. Acta Geol. Sin. Engl. Ed. 90 (6), 2275–2276.

Zhu, J.C., Li, R.K., Li, F.C., Xiong, X.L., Zhou, F.Y., Huang, X.L., 2001. Topaz-albite granites and rare-metal mineralization in the Limu District, Guangxi Province, southeast China. Miner. Dep. 36 (5), 393–405.

Zou, Y.Q., Chen, X.L., Huang, W.T., Zhang, J., Liang, H.Y., Xu, J.F., Chen, L., 2017. Identification of an Early-Middle Jurassic oxidized magmatic belt, south Gangdese, Tibet, and geological implications. Sci. Bull. 62 (12), 888–898.